*International Journal of Satellite Communications and Networking*

WILEY

SPECIAL ISSUE PAPER OPEN ACCESS

# Photonic Integrated Circuits for Optical Satellite Links: A Review of the Technology Status and Space Effects

Giulio Terrasanta[1,2] | Marcin Wojciech Ziarko[1] | Nicola Bergamasco[1] | Menno Poot[2,3,4] | Juraj Poliak[1]

[1]Institute for Communications and Navigation, German Aerospace Center (DLR), Oberpfaffenhofen, Germany | [2]Department of PhysicsTUM School of Natural Sciences, Technical University of Munich, Garching, Germany | [3]Munich Center for Quantum Science and Technology (MCQST), Munich, Germany | [4]Institute for Advanced Study, Technical University Munich, Garching, Germany

**Correspondence** Giulio Terrasanta (giulio.terrasanta@dlr.de)

**Received:** 22 January 2024 | **Revised:** 26 July 2024 | **Accepted:** 14 January 2025

**Keywords:** free space optical communications | photonic integrated circuits | radiation effects | satellite communications

## ABSTRACT

Optical satellite communications provide high-data rates with compact and power efficient payloads that can solve the bottlenecks of RF technologies. Photonic integrated circuits have the potential to reduce the cost, size, weight, and power consumption of satellite laser communications terminals, by integrating all the required photonic components on a chip. This can be achieved by leveraging on the mature technology for fiber communications. In this article, the technology status of photonic integrated circuits for optical satellite link is reviewed. Different material platforms are compared, with a focus on high-speed coherent optical communications. The integration of the photonic chip into a communications payload is discussed, together with possible challenges and opportunities. The impact of the space environment, especially the one of radiation, on the performance of the integrated photonic devices is reviewed and discussed.

## 1 | Introduction

Optical technologies play a key and crucial role in today's communications. Terrestrial systems, such as long-haul fiber-optic networks, have been able to keep up with the exponential growth of the Internet data rates by developing novel, and more sophisticated solutions. Among these, photonic integrated circuits (PICs) are one of the enabling technologies to achieve high performance while reducing power consumption and system footprint. First conceived in 1969 [1], their evolution closely resembles that of electronic ICs. While in the beginning only a single component per chip was possible, nowadays thousands of different functionalities can be integrated on a single chip [2]. For instance, state-of-the-art PICs enable Tb/s capacity by monolithically combining tens of active and passive components [3, 4]. Furthermore, in recent years, the rapid development of this technology has led to the establishment of open-access commercial foundries [5, 6]. These allow any user to design and fabricate PICs, taking advantage of the library of device designs already available, without the need of developing and establishing a fabrication process. Contrary to electronic integrated circuits (ICs), where Si is the dominant material platform, many different technologies are available for PICs, such as indium phosphide [7, 8], silicon [5], or silicon nitride [9]. Since the development of PICs has been driven primarily by their application in fiber optic communications, the available foundries can offer, among others, the key building blocks for advanced high-speed optical transceivers, such as high-speed modulators and photodetectors [6, 10]. These key blocks could now benefit other applications, such as optical satellite links (OSLs) for high throughput communications, time transfer, and ranging.

The interest in optical satellite communications has grown rapidly in recent years [11–15]. Thanks to the high data rates provided by optical links [16–18], satellite networks based on OSLs have the potential to unlock the spectral bottleneck that RF technologies are facing nowadays [11, 15]. Furthermore, they can complement the existing fiber network, and provide global

broadband access. The currently demonstrated laser communications systems for satellites are built using discrete optical components, meaning that the employed devices are packaged separately, and inter-connected via fibers. Since satellite payloads are limited in terms of size, weight and power consumption (SWaP), miniaturization and integration of components benefits the entire system, thus reducing the overall cost and SWaP (C-SWaP) of the optical communications terminal [11, 19]. Furthermore, the use of PICs gives access to other physical processes, such as microresonator-based combs, which can be used for massively parallel optical communications [20, 21]. Another advantage is that PICs are less sensitive to external perturbations compared to the discrete counterparts, thus making them suitable for the challenging space environment [11]. However, space-based PICs are still a novel topic of research. Space-based systems face a number of challenges that are different from terrestrial-based systems. First of all, the environment itself is fundamentally different, due to radiation and temperature fluctuations experienced by an orbiting spacecraft. These can degrade and/or change the performances of regular terrestrial optical transceivers. For instance, results show that the radiation the spacecrafts experience on orbit can shift the wavelength of a laser [22], and increase losses in waveguides [23]. Second, the system requirements for an OSL are different from those of a fiber-based link, due to the different channel properties. For instance, the Doppler effect caused by the satellite movement needs to be accounted for not only in the transceiver design, but also for allocating the bandwidth in a wavelength division multiplexing (WDM) channel. Another challenge is the temperature cycling experienced by the payload during the spacecraft orbit. Since the components are integrated in a small volume, the thermal power density is increased, thus making more complicated to keep the operational temperature stable [24]. Therefore, targeted developments are needed to adapt the current terrestrial PIC technology to OSL.

In this paper, we provide a comprehensive review of the latest technological developments towards the integration of bulk optical components into PICs for OSL applications. In the first part, we will analyze the available materials and devices that could be used for OSLs. We will also discuss possible strategies for integrating PICs into an OSL terminal and present current challenges and opportunities. In the second part, we will report on the environmental tests that have already been performed on PICs, with a focus on radiation. The three main categories of radiation tests are reported, compared, and analyzed, namely, total ionizing dose (TID) effects, displacement damage (DD) effects, and single event effects (SEE). Finally, conclusions are drawn from the discussed topics.

## 2 | Technology Review

PICs have been a tremendous technological advancement in the field of optics and photonics. The integration of numerous optical functions has found applications in a wide range of fields, from high-speed data communications, to quantum computing and sensing. In optical communications, PICs allowed to integrate the needed components, such as modulators, lasers, and photodetectors, on a single chip, instead of having separate devices interconnected by fibers. This section discusses the technology status of PICs, but with the specific focus on using this platform for OSLs in the C-band (1530–1565 nm). Although there are three main free-space optical telecommunication wavelength ranges around 810, 1064, and 1550 nm that are not strongly absorbed by the atmosphere [25], most commercial components, and PICs, have been developed for fiber communications in the C-band [25]. First, we will give a brief introduction to PICs for the reader unfamiliar with the topic. The different technology material platforms are discussed in the second subsection. Then, we discuss the use of PICs in the context of OSLs, including recent experiment involving PICs for free space optical communications. Finally, current challenges and opportunities are discussed.

### 2.1 | PICs: Brief Introduction

PICs can be seen as the optical counterparts of electronic ICs. An electronic IC is a semiconductor chip on which multiple electronic components, such as transistors, resistors, and capacitors, are fabricated together and interconnected by conductive traces. Similarly, a PIC is a chip on which optical components are integrated and interconnected by waveguides. In contrast with electronic IC, where the signal is an electrical one made up of electrons, a PIC transports and modifies an optical signal made up of photons. A complete history of this technology can be found in [2], of which we summarize some key steps here. The concept of PIC was first proposed in 1969 [1], but the technology had limited commercial success for the first 40 years. However, with the introduction of optical networks, this technology played a crucial role in scaling the optical communication bandwidth, and the last two decades have seen an exponential growth of PICs, both in terms of the number of components per chip and of the data capacity per chip. Today, this technology has reached a maturity that allows for open-access commercial foundries [5, 6]. As an example, Figure 1 shows a photograph of an indium phosphide PIC fabricated through such a commercial foundry. This shows a 8 mm × 2 mm InP chip designed for OSLs [19]. The chip contains multiple optical components, including two

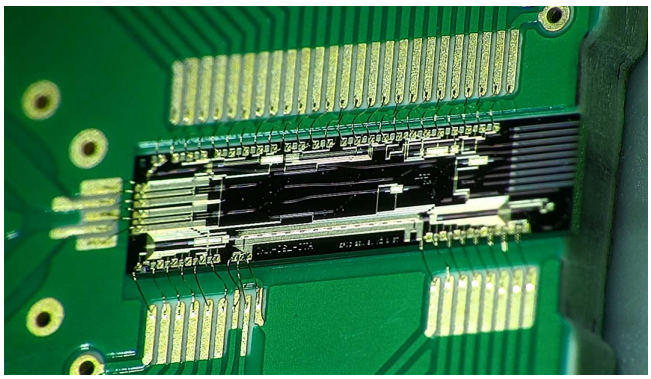

**FIGURE 1** | A 2 mm × 8 mm InP PIC (black) fabricated in a commercial foundry, integrating an optical transceiver designed for OSLs [19]. The chip is glued on a printed circuit board (green). Electrical connections (gold) between the PIC and the board are made via wire-bonding. Light coupling from/to the PIC is achieved via edge coupling, using the nine spot size converters (gray) on the right edge of the PIC in combination with a fiber array.

laser sources, a Mach-Zehnder modulator, two pairs of balanced photodetectors, two photodetectors, a 90° hybrid, and many splitter and combiners. All of these are interconnected by optical waveguides. Compared to using discrete components, where each one of these devices would be a separate package with fiber connectors, everything is monolithically integrated onto a single chip. As we will see later, some material platforms for PICs are compatible with the fabrication processes of electronic ICs, and thus also the electronic components could be integrated on the same chip as the optical ones. The chip shown in Figure 1, as for any bare chip, needs to be interfaced with the outer world; that is, it needs to be packaged. A packaging review can be found in [26], where different packaging strategies for PICs are discussed.

## 2.2 | Material Platform

PICs can be fabricated on a variety of different material platforms that exhibit different optical and electrical properties. Therefore, the functionalities and performance requirements of a specific application are critical in the choice of the technology platform. Especially when fabrication relies on a commercial foundry, the choice of the material also limits the available devices that can be integrated. For instance, lasing and amplification cannot be achieved by using silicon. Nevertheless, in the recent years there has been a strong growth of hybrid photonic circuits, that is, integration of chips of different materials, and the technological challenges such as optical interconnection and packaging are being addressed [27]. This solves the problem of being limited to the performances of one platform alone, and allows to integrate the best of each material. We will now discuss different material platforms available to fabricate components for high-speed satellite optical communications. This discussion focuses on the key properties that are needed for high-speed OSLs in the C-band. A non-application specific comparison of the materials, that includes properties such as refractive index and bandgap, can be found in [27].

The main material platforms that are available through open-access services are indium phosphide (InP) [6], silicon (Si) and silicon nitride (SiN) [28], and silicon dioxide ($SiO_2$). $SiO_2$ can only be used for passive devices, and it is excluded from the discussion because active devices, such as modulators and lasers, are the critical components of an optical communications system. Si is a semiconductor with a high refractive index. It is compatible with complementary metal-oxide-semiconductor (CMOS) processes, allowing for monolithic integration with electronics and for fabrication in standard CMOS foundries. The latter is a major advantage in the development of Si photonics (SiPh) PICs, because it allows access to mature, low-cost, and high-yield fabrication processes [10]. Another platform that is compatible with CMOS processes is SiN. Compared to Si, it has a wider transparency window and lower optical loss, which can be used for applications ranging from the visible to near-infrared wavelengths. InP is a compound semiconductor and, among these four materials, the only one with a direct bandgap. This means that it can be used to fabricate devices where light is emitted and absorbed by carrier recombination in the bandgap. In other words, it is the only platform on which lasers can be fabricated, thus making it of critical importance to an optical communications system.

Another material platform that is worth mentioning is lithium niobate ($LiNbO_3$). $LiNbO_3$ is a ferroelectric material with strong electro-optic properties, and it is commonly used in the fabrication of discrete modulators. Recent advances in the fabrication of thin-film $LiNbO_3$ have enabled the fabrication of thin-film lithium niobate on insulator (LNOI) chips. However, LNOI is still not a competitive integrated platform due to the non-mature fabrication techniques [29]. The development of a first European LNOI foundry has only very recently started [30].

The key properties are listed in Table 1. For each material platform, a colored grade (**+**, **O**, and **–**) is provided to indicate whether a property is well-satisfied, partially-satisfied, or not available in the material platform, respectively. While we could have provided state-of-the-art values here, such values are usually not the ones provided by commercial foundries, and even different foundries can have significantly different values. For example, different SiPh foundries can provide maximum detector bandwidths ranging from 35–60 GHz, and waveguide losses ranging from 0.9 to 2.5 dB/cm [10]. The key properties are now discussed:

- **Waveguide loss**: Waveguides are the basic building block of any PIC, as they connect the integrated devices. The waveguide loss is thus important to minimize the reduction in the optical signal power from one device to another and thus the total loss at the transmitter and receiver side. Optical satellite links typically operate on a tight optical power budget, with a link margin such as 2 dB [15], so keeping the losses low is important for an OSL system. Of the materials mentioned, SiN and LNOI have the lowest losses, typically in the order of 0.01 dB/cm [10] and 0.1–0.01 dB/cm

**TABLE 1** | Key properties comparison for high-speed optical communications among different technology platforms.

| Property | InP [6] | SiPh [10, 28] | SiN [10, 36] | LNOI [29, 31] |
|---|---|---|---|---|
| Waveguide loss | O | O | + | O |
| Optical gain/ amplification | + | — | — | — |
| Photodetector | + | + | — | — |
| Fiber coupling | **O** | **O** | + | **O** |
| Polarisation independence | **O** | — | **O** | — |
| RF modulation | + | + | — | + |
| CMOS compatibility | — | + | + | **O** |
| Footprint | — | + | **O** | **O** |
| All-in-one | + | **O** | — | — |
| Open access MPWs | + | + | + | **O** |

*Note:* The grades (**+**, **O**, and **—**) indicate whether a property is well-satisfied, partially satisfied, or not available in the material platform, respectively.

[31], respectively, as opposed to SiPh and InP, which are on the order of 1 dB/cm [6, 10].

- **Optical gain/amplification**: Optical amplification can only be realized in materials with a direct bandgap, which in this case is only InP. InP semiconductor optical amplifiers (SOAs) can be used to realize amplifiers, or lasers when combined with a feedback mechanism. Having a light source is fundamental on the transmitter side, and is also required on the receiver side for coherent communication. Therefore, InP is always needed, either as a standalone PIC or in combination with other platforms.
- **Photodetector**: High-speed photodetectors (PDs) are needed on the receiver side, in order to convert the optical signal into an electrical one. Bandwidths in the tens of GHz range can be achieved in both InP and SiPh, employing InGaAs and Si-Ge PDs, respectively.
- **Fiber coupling**: Loss due to the fiber coupling is another important metric and contributes to the total link loss. Every PIC needs to be interfaced with the overall optical system by coupling the optical mode of the waveguide to the optical mode of a connected fiber. This interface is typically lossy, and the loss depends on how accurate the mode matching is.
- **Polarization independence**: Available integrated devices are typically optimized to work with a specific light polarization, thus not being polarization independent. This limits the possibility of employing dual-polarization modulation formats. A typical workaround is to use polarization rotators. However, integrated devices for polarization control are challenging to fabricate [32] and not available for all foundries.
- **RF modulation**: High-speed modulation is essential for optical communications. Thanks to electro-optic effects, bandwidths of tens of GHz can be achieved in InP, SiPh, and LNOI. For instance, a 15-GHz InP modulator realized in a commercial foundry was presented in [33], allowing for 80-Gbps operation. SiN modulators rely on thermal effects that limit the bandwidth to the kHz range, which is not enough for high-speed optical communications.
- **CMOS compatibility**: Integration with CMOS processes is an incredible advantage, allowing access not only to high-yield and low-cost manufacturing but also to monolithic integration with electronic ICs. Only SiPh and SiN are CMOS compatible.
- **Footprint**: The footprint of a material platform is given by how small the integrated photonic devices can be fabricated. This is determined by the optical confinement, which in turn is given by the contrast between the refractive indices of the waveguide and its surroundings. The larger the difference, the stronger the confinement. Among the discussed platforms, Si has the strongest confinement.
- **All-in-one**: The only material platform that satisfies all the requirements is InP, that is, the only technology where a transmitter/receiver can be realized with monolithic integration, at the cost of a large footprint and incompatibility with CMOS processes. The other platforms do not provide lasing and amplification, and thus always need to be paired with an external source or an InP die.
- **Open access foundries**: Having access to a commercial foundry allows to take advantage of already existing processes and knowledge, without having to develop one own fabrication. InP, Si, and SiN have several commercial foundries available. Recently, development towards the first LNOI commercial foundry have also been made [34, 35].

From this brief comparison, it is evident that there is a trade-off in between the different platforms when selecting a material for integrating OSL systems into a PIC. InP is the only material that can handle all the required components at the cost of footprint, CMOS compatibility, and loss. Therefore, a combination of multiple material platforms might often be the only way to maximize the performance [37]. As an example, the low loss of SiN can be used together with the optical gain of InP to realize extremely narrow-linewidth lasers [36]. Furthermore, one might consider employing different technology platforms for different subsystems of the OSL terminal. For instance, SiN could be used for (de)multiplexing and filtering the transmitted/received optical signal, while InP is used for the optical signal generation, modulation, and detection.

### 2.3 | PIC Integration Into Optical Space Communications Terminal

The system architecture of an OSL payload depends on the modulation format that is employed. For example, it differs if coherent modulation (phase and intensity) is used, or intensity modulation. Another difference would be if the system uses wavelength division multiplexing. Figure 2 shows a high-level block diagram of a OSL terminal, where some blocks are generic (i.e., receiver and transmitter) to fit any possible implementation.

The incoming optical beam is collected by the telescope and coupled into a fiber in the laser communications terminal. The fiber-coupled optical signal is then filtered, pre-amplified, and demultiplexed into the different wavelength channels. If a single wavelength channel is used, then no demultiplexer is needed and the optical signal is directly coupled to the single receiver. The optical signals are then converted to electrical ones using the optical receiver. On the transmitter side, the optical signal is generated and modulated according to the employed modulation format. The different wavelength channels are then combined in the multiplexer, when WDM is used, amplified in the erbium-doped fiber amplifier (EDFA), and transmitted through the telescope with the inverse steps of the received beam.

Since the focus of this paper is on the key-components for OSLs based on coherent optical communication, we illustrate this with the receiver and transmitter architectures for polarization-division multiplexed quadrature phase-shift keying (PDM-QPSK) in Figure 3. This coherent modulation format is popular in fiber-optics for its spectral efficiency, and it provides an overview of how the key on-chip components are used in this type of system. For a coherent receiver, the block includes several components, such as a polarization splitter and rotator, a laser, two 90° hybrids,

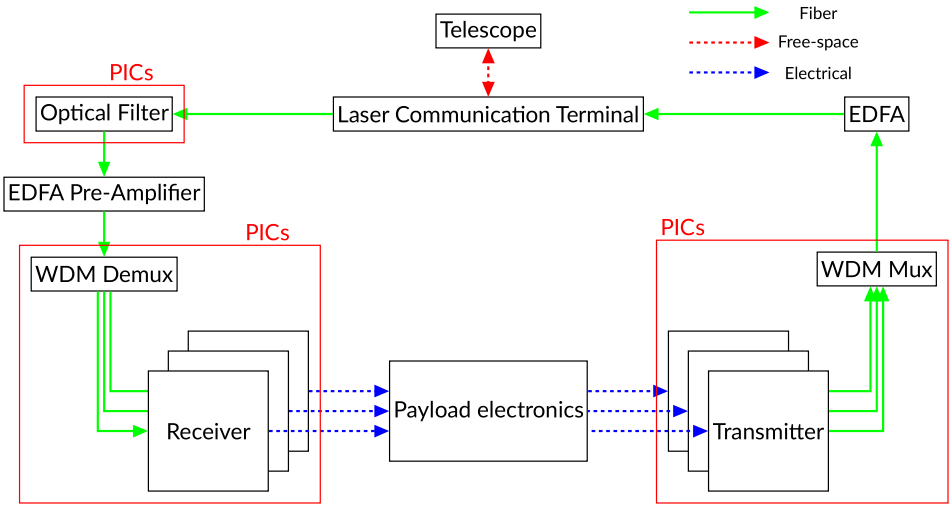


**FIGURE 2** | Block diagram of satellite/ground station laser terminal highlighting potential PIC subsystem integration. A WDM system is shown. If a single wavelength channel is used, then a demultiplexer (multiplexer) is not needed and the optical signal is directly coupled to the single receiver (transmitter). EDFA, erbium-doped fiber amplifier; WDM, wavelength division multiplexing.

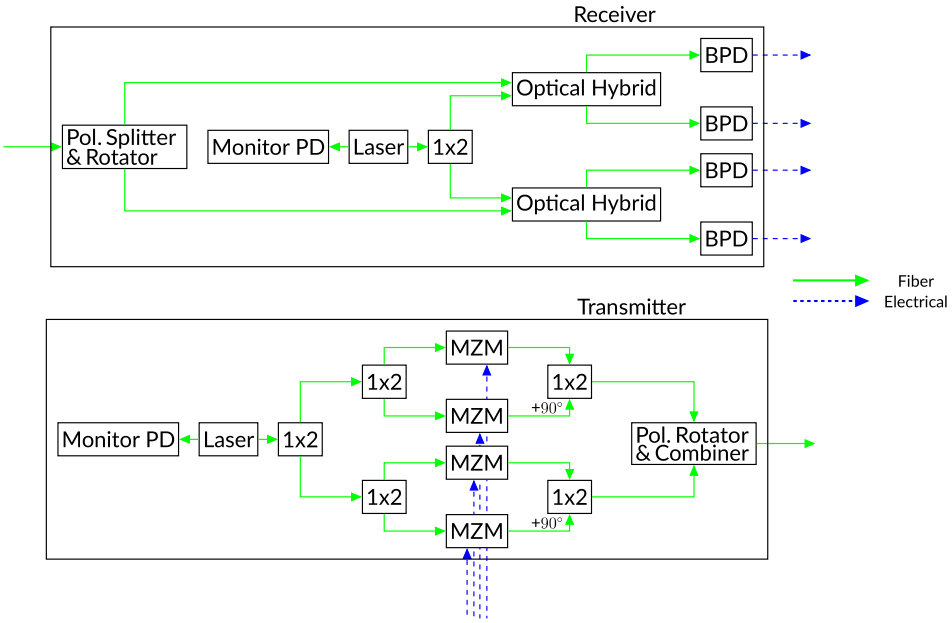


**FIGURE 3** | Block diagram of possible architectures of an integrated receiver and a transmitter for PDM-QPSK. +90°, 90° phase shift; 1 × 2, one by two splitter; BPD, balanced PD; MMI, multi-mode interferometer; MZM, Mach-Zehnder modulator.

and four balanced PDs. On the transmitter side, a laser, four modulators, and a polarization rotator and combiner are used.

Figures 2 and 3 highlight that many different optical components need to be used, which could benefit from integration on one or multiple PICs. The integration strategy is driven by many different factors, such as system requirements, and material selection. On the receiver side, $n$ InP chips could be used for the $n$ receivers. An additional chip could be used for the WDM demux, for instance, by using arrayed-waveguide gratings (AWGs) based on SiPh [38], SiN [39], or InP [40]. The $n+1$ approach makes the system architecture scalable with the number of channels $n$. The receiver subsystem could also be integrated into two chips, one chip for the demultiplexing and one InP chip with all the receivers, making it more compact but more challenging to extract all the electrical signals out from the single InP chip. Another option would be to have a single InP chip: Here, the advantage of monolithic integration comes at the cost of a lossy and large WDM demux. A similar reasoning applies to the transmitter subsystem, which could also be integrated in $n+1$ chips, in the case of $n$ separate transmitters and one multiplexer, or two chips, one integrating all the transmitters and one multiplexer, or a single monolithic chip. In addition, the optical filtering on the receiver side could also be integrated into a PIC. In principle, also the EDFA pre-amplifier could potentially be replaced by a SOA, but the noise level in currently available SOAs is higher than in EDFAs [41].

Some studies have already employed PICs in free-space optical communications systems, thus demonstrating the potential of using this technology also for OSLs. In [42], the transmitter side of the link was integrated into an InP chip. The transmitter chip consisted of a sampled grating distributed Bragg reflector (SGDBR) laser, two SOAs, and a MZM. The laser is tunable in the C-band with 44 nm of tuning range, it has a side mode suppression ratio (SMSR) of 55 dB, and a linewidth of 6.4 MHz. The two SOAs are used to compensate for the modulator insertion loss, and to boost the output power to 14.5 dBm. The signal from the PIC was collected by a single mode fiber, coupled to an optical collimator, transmitted in air, and collected by another collimator. The fiber-coupled signal is first attenuated to emulate the loss in a free-space link and then amplified with an EDFA to recover part of the lost power. Non-return-to-zero on-off keying (NRZ OOK) modulation at 1 and 3 Gbps was tested. Error free transmission was shown up to 300 m (28 dB of attenuation) with 3 Gbps and up to 400 m at 1 Gpbs. Longer distances could be achieved with a booster-EDFA at the transmitter side, which is typically used in OSLs.

In [43], another InP transmitter was presented, consisting of a SGDBR laser, a SOA, a MZM and an electro-absorption modulator (EAM). The authors showed that the chip is suitable for optical satellite communications by measuring data rates up to 10 Gpbs in NRZ-OOK and DPSK modulation at the output of the chip. Nevertheless, the chip was not tested with a lossy channel.

### 2.4 | Challenges and Opportunities

While PICs offer a large number of benefits and advantages over the use of discrete optical devices for satellite-based optical communications, they also face a number of challenges. Some of these limitations are in common with terrestrial fiber communications systems. For example, a number of functionalities are currently not possible to be fully integrated on a chip. Three building blocks that are needed once per payload and that are not available on PICs are very high-power amplifiers (> 10 W output power), optical isolators, and circulators. In the case of the first functionality, external fiber amplifiers, such as EDFAs, are employed as booster amplifiers in the OSL. There is ongoing research to address this functionality gap by either designing high-power SOAs [44, 45] or introducing Erbium-doping on a chip to form Erbium-doped waveguide amplifiers (EDWAs) [46, 47]. While both have made recent progress in terms of their performance, the power levels are still not sufficient for OSL applications. Optical isolators and circulators are another important functional block that is not currently ready for PIC integration. These devices are required to avoid potential problems with back-reflections into sensitive components, such as lasers, arising from PIC interfaces that can ultimately lead to performance degradation of the entire integrated system. While this is important for classical communications, it can be of even higher importance in case of the quantum key distribution (QKD) systems, where receivers work in the photon-counting regime and thus additional photons due to back-reflection result in errors. Currently, the isolator functionality has to be implemented off the chip with the use of external components such as magneto-optic crystals. However, recent developments in the field can lead in the near future to on-chip implementations [48].

There are also a number of additional challenges for PICs resulting directly from the application in satellite-based optical communications. In this paper, the focus is placed on the exploration of the impact of the environmental factors such as radiation, temperature and mechanical shocks. All these phenomena and the resulting effects on the PIC need to be accounted for in order to design an operational system. Furthermore, in some optical link scenarios, additional effects, such as Doppler shift due to satellite relative movement, need to be considered in the design of the optical system elements including sources, filters, and coherent receivers.

Here, the primary focus is placed on satellite-based coherent optical communications systems and the on-chip components that are required for this application. However, one should keep in mind that PICs can be also employed in a number of other satellite systems that go beyond the optical communications field. As discussed in [49], PICs could also be employed in space system the fields of sensing, biological applications, autonomous navigation and positioning, as well as imaging. The same or similar integrated devices can be used in applications such as time transfer and ranging [50], LiDAR [51, 52], optical gyroscopes [53], spectroscopy [54], and atmospheric turbulence compensation [55]. Moreover, integrated photonics can also employed in RF communications payloads with microwave photonics [56, 57], for instance to achieve beamforming, filtering, or up and down-conversion. Furthermore, there are also relevant new optical functionalities that become more easily available through photonic integration, as is in the case of frequency combs [58] and photonic lanterns [59].

## 3 | Space Environmental Effects

The development of integrated photonic devices for optical communications has been driven primarily by fiber-optic communications. As a result, the performance of such devices has been carefully optimized to operate in the terrestrial environment. The space environment is very different and presents additional complications and challenges to any space system. While the impact on electronic systems has been studied for decades [60], the impact on integrated photonics is a new topic of research and there are still many open questions [49, 61, 62]. The main focus of this section is the effect of space radiation, and it will be covered in the first and main part. The results described are derived not only from space-oriented systems, but also from systems designed for terrestrial environments with high levels of radiation, such as the Large Hadron Collider (LHC). Afterwards, other challenges of the space environment, such as thermal management, vibration, and lifetime, are briefly discussed.

### 3.1 | Radiation Effects

Radiation studies are generally divided into three categories: total ionizing dose (TID) effects, displacement damage (DD) effects, and single event effects (SEEs). It is important to emphasize that, even though the three effects are studied independently, they can all be caused by the same radiation event [62] and thus occur at the same time. A detailed description of

these three effects, including the radiation sources involved, damage mechanism, microscopic effect, and the macroscopic effect on photonic devices can be found in [63] and [62]. Here we briefly summarize the key information:

- **TID**: it is a cumulative effect, meaning that the radiation dose increases over the satellite mission duration. It consists of an accumulation of charges at the material surface/interface. It typically results in surface oxidation, carrier population increase, and bulk trapped charges [62]. These are typically studied using X-ray sources or cobalt-60 radiation sources. To qualify a component for space applications, testing at radiation doses between 1.5 krad and 1500 krad is expected [64].
- **DD**: also a cumulative effect, it results in the displacement of atoms from the material, thus creating defects and carrier recombination centers [62]. DD effects are typically studied using two radiation sources: neutrons or protons. As discussed in [65], neutrons cause only non-ionizing damage, and thus are an important radiation test to focus only on DD; however, protons are the most abundant radiation source in the near-Earth space environment [66], and generate both TID and DD. Both neutron and proton studies will be considered here. Fluences applied during DD testing and qualification are typically in the order of $10^{10}\,\mathrm{cm}^{-2}$ to $10^{12}\,\mathrm{cm}^{-2}$ [63].
- **SEE**: this effect is transient, meaning that the material recovers after a period of time during which the properties are affected. It results in charge generation and a temporary increase in carriers in the material [62]. This effect is typically tested with heavy ions. Typically, for a specific ion with a speficic energy, the test is conducted until 100 events are recorded or until a fluence of $10^{12}\,\mathrm{cm}^{-7}$ is reached, which is sufficient for most environments [63]. Another technique is to employ high-energy lases pulses. The laser-induced SEE also results in a transient increase in carriers in the material, but with a different distribution compared to an actual ion strike.

We will now look into the impact of these three radiation effects on four categories of integrated devices that are important for optical communications: passive devices, modulators, lasers and amplifiers, and photodetectors.

### 3.1.1 | Waveguides, Resonators, Mach-Zehnder Interferometers

The effect of radiation on passive devices such as waveguides, ring resonators (RRs), and Mach-Zehnder interferometers (MZIs) can be reduced to a change in the optical properties of the material. This results in different refractive index and absorption losses that change the characteristics of the devices. In this respect, RRs and MZIs are based on interference and are therefore particularly sensitive to any change. Therefore, it is of interest to compare studies on these devices, even if they are different, as they indicate how a specific material platform responds to radiation. While it may be more relevant for optical communications to immediately look at key devices such as MZMs and PDs, this first step is critical because the fundamental change in optical properties is at the root of the radiation effects on any device.

Ring resonators are characterized by resonances that occur when the length of the resonator is equal to an integer number $m$ of wavelengths in the medium, that is, $2\pi R = m\lambda_r/n_{\mathrm{eff}}$. Similarly, the spectrum of MZIs is characterized by dips that occur when there is destructive interference between the optical signal in the two arms. When the effective refractive index $n_{\mathrm{eff}}$ of the waveguide changes due to radiation, the wavelength of such resonances and dips shifts. The shift of such resonances $\Delta\lambda$ can be used to infer $\Delta n_{\mathrm{eff}}$ using [67]

$$\Delta n_{\mathrm{eff}} = \frac{n_g \Delta\lambda}{\lambda_r}, \tag{1}$$

where $\lambda_r$ is the vacuum wavelength of the considered resonance, and $n_g$ is the group index, which can be determined with

$$n_g = \frac{\lambda_r^2}{\mathrm{FSR} \cdot L}. \tag{2}$$

Here, FSR is the free spectral range of the resonances and $L = 2\pi R$ is the resonator length. These equations are also valid for MZIs, where $L$ is the arm imbalance length, that is, the difference in length between the two arms of a MZI. These equations are used in the following analysis to compare different studies.

**3.1.1.1 | TID.** First, we compare the measured difference in effective refractive index $\Delta n_{\mathrm{eff}}$ in the TID studies. Since not all of them directly report $\Delta n_{\mathrm{eff}}$, we use Equation (1) to convert the reported $\Delta\lambda$ to $\Delta n_{\mathrm{eff}}$. [68] also required a simulation of $n_g$ that was performed with Rsoft.

Figure 4a shows a comparison of the following materials: InP, Si, SiN, amorphous silicon[1] (a-Si), $SiO_2$, and $LiNbO_3$. First, we can see that both an increase and a decrease of $n_{\mathrm{eff}}$ are possible, corresponding to a red and blue shift of the resonances, respectively. More specifically, Si shows a negative shift in most studies, while InP, SiN, and a-Si show a positive shift. Among the latter, InP is the most sensitive to TID, with a significant increase after 1e5 rad. Another thing to note is the effect of cladding and waveguide dimensions, which can drastically change the effect of ionization. A direct quantitative comparison of the results is not trivial, especially due to the different radiation sources used, typically $\gamma$-ray or X-ray, and the different radiation doses. However, a qualitative analysis and comparison of these studies can be made. To understand the results, several aspects should be considered. The first is the effect of TID on the materials themselves, that is, the change in refractive index $\Delta n$. The second aspect is to consider the combination of $\Delta n_{\mathrm{core}}$ and $\Delta n_{\mathrm{cladding}}$ to the total $\Delta n_{\mathrm{eff}}$. In other words, what is the total result of the changes in the waveguide material and in the material surrounding the waveguide. Last but not least, the presence of a cladding on top of the waveguide needs to be considered. These three effects are now discussed in detail.

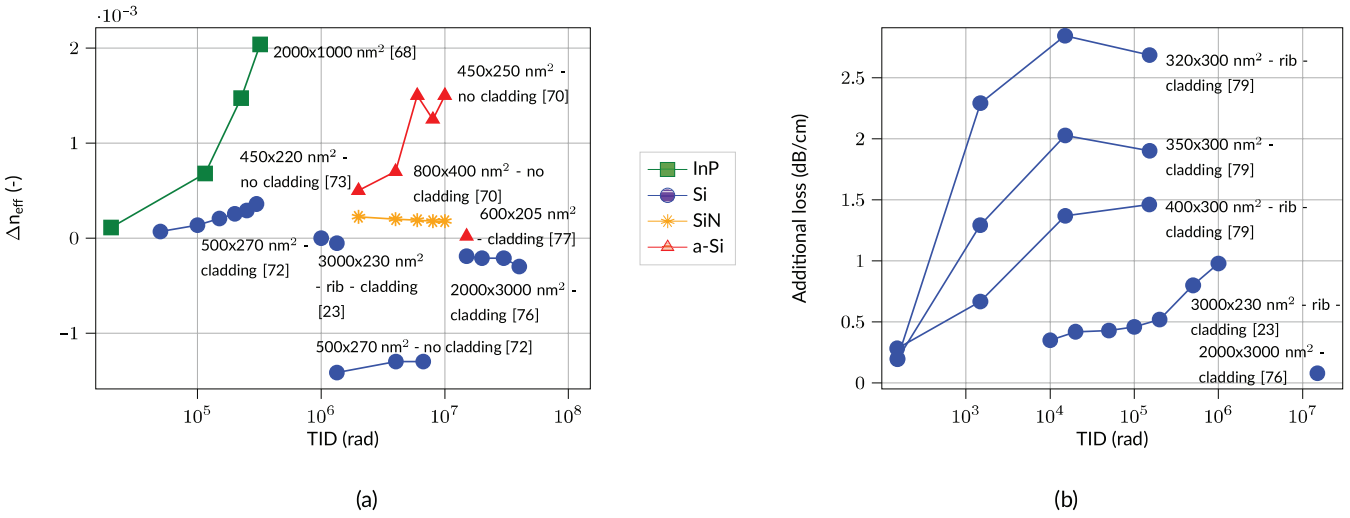


**FIGURE 4** | Summary of (a) $\Delta n_{\text{eff}}$ and (b) additional losses due to TID in different material platforms. Waveguide dimensions (width and height), presence of cladding, and reference are noted next to the plots. *Strip/ridge* waveguides are considered, unless *rib* is noted in the description; in this case, the waveguide dimension are strip width and total thickness (slab+strip). The $\Delta n_{\text{eff}}$ is either given directly in the reference or inferred using Equation (1) and 2 with the available data. Only [68] required a simulation of $n_g$ that was performed with Rsoft.

The damage $\Delta n$ is the result of a combination of different microscopic processes, namely, surface oxidation, trapped charges and defects, and volume compaction or expansion [62]. The presence of multiple processes has been clearly demonstrated and explained by Du et al. [70], where a-Si and SiN were exposed to ionizing radiation in both air and argon (Figure 4a shows the air results). When ionized in argon, both a-Si and SiN show a strong increase in $n_{\text{eff}}$. Instead, this trend is different in air, and $\Delta n_{\text{eff}}$ of a-Si has a saturation for a TID of 6 Mrad, and $\Delta n_{\text{eff}}$ of SiN has a decreasing trend. This has been attributed to surface oxidation, which is now possible due to the presence of oxygen: silicon dioxide has a lower refractive index than Si and SiN, so surface oxidation reduces $n$. Another study that shows that there are various competing mechanism is [71], where the authors extracted $\Delta n_{\text{eff}}$ by using a microbeam X-ray to target a specific arm in a MZI with $450 \times 220\,\text{nm}^2$ cladded Si waveguides. The data are not shown in Figure 4a due to the much higher dose (1e9–1e12 rad) used in this study. At first, $\Delta n_{\text{eff}}$ is negative, which was attributed to oxidation. This negative trend eventually stops, because the cladding limits the available oxygen. At high doses, above 4e11 rad, $\Delta n_{\text{eff}}$ is positive, meaning that a competing process has reverted the previous negative shift. Radiation-induced compaction was considered as the likely cause of this positive trend. Another similar study was performed in [72]. Also in this case, a $SiO_2$ cladding is used to stop surface oxidation, which allows to prevent the blue shift otherwise experienced by the devices without cladding. Similarly to [71], $\Delta n_{\text{eff}}$ shows a saturation after the initial decrease, which was motivated by a saturation of the oxidation process beyond the native oxide. Another interesting feature of Figure 4a is that both positive and negative $\Delta n_{\text{eff}}$ were reported for similar unclad Si waveguides [72, 73]. Therefore, the dominant microscopic process also seems to be determined by the applied dose rate and total dose. Dumon et al. [73] and Bhandaru et al. [72] used two very different dose rates and total doses, 105 rad/min up to 300 krad [73] and 44.7 rad/min up to 6705 krad [72], respectively. Dumon et al. [73] measured a positive $\Delta n_{\text{eff}}$, which was attributed to defects. Instead, Bhandaru et al. [72] measured a negative $\Delta n_{\text{eff}}$, attributed to surface oxidation.

The second aspect that determines $\Delta n_{\text{eff}}$ is now considered, namely, its relationship to $\Delta n_{\text{core}}$ and $\Delta n_{\text{cladding}}$. In a waveguide, $n_{\text{eff}}$ can be intuitively understood as the average of its $n_{\text{core}}$ and $n_{\text{cladding}}$, weighted by the optical mode overlap with the core and cladding regions. As an example, the simulation of the optical field profile in two Si waveguides is shown in Figure 5. The resulting $n_{\text{eff}}$ is lower for the waveguide in Figure 5a compared to the one in Figure 5b due to the lower confinement, thus higher overlap with the low-index $SiO_2$. This also shows that lower confinement results in more overlap with the waveguide surface where trapped charges accumulate and surface ionization occurs. $\Delta n_{\text{eff}}$ can be described as [74]

$$\frac{\Delta n_{\text{eff}}}{\Gamma_{\text{core}} + \Gamma_{\text{clad}}} = \frac{\Gamma_{\text{core}}}{\Gamma_{\text{core}} + \Gamma_{\text{clad}}} \Delta n_{\text{core}} + \frac{\Gamma_{\text{clad}}}{\Gamma_{\text{core}} + \Gamma_{\text{clad}}} \Delta n_{\text{clad}}, \quad (3)$$

where $\Gamma_{\text{core}}$ and $\Gamma_{\text{clad}}$ are the optical mode confinement factors in the core and cladding, respectively. By varying the dimension of a silicon carbide[2] (SiC) waveguide in $SiO_2$, Du et al. [74] showed the validity of this equation and that it is possible to extract separately $\Delta n_{\text{eff}}$, $\Delta n_{\text{SiC}}$, and $\Delta n_{\text{SiO}_2}$. Furthermore, they showed that it is possible to optimize the confinement factor to have a radiation-hardened waveguide by taking advantage of the opposite signs of $\Delta n_{\text{SiC}}$ and $\Delta n_{\text{SiO}_2}$. Using a similar approach, Zhou et al. [76] showed that a wide and thick Si waveguide can be used at very high radiation dose with only a small change in $n_{\text{eff}}$ due to the extreme confinement of the optical mode, and thus small overlap with the carrier accumulation and oxidation occurring at the interface with the surrounding material.

In terms of TID-induced absorption losses, which is the second and complementary side of the change in optical properties, most of the previously mentioned studies did not find an increase in losses. For example, no significant additional loss was measured in InP [68], Si [72, 73], SiN [70], a-Si [70, 77], SiC [74], and $SiO_2$ [78]. This

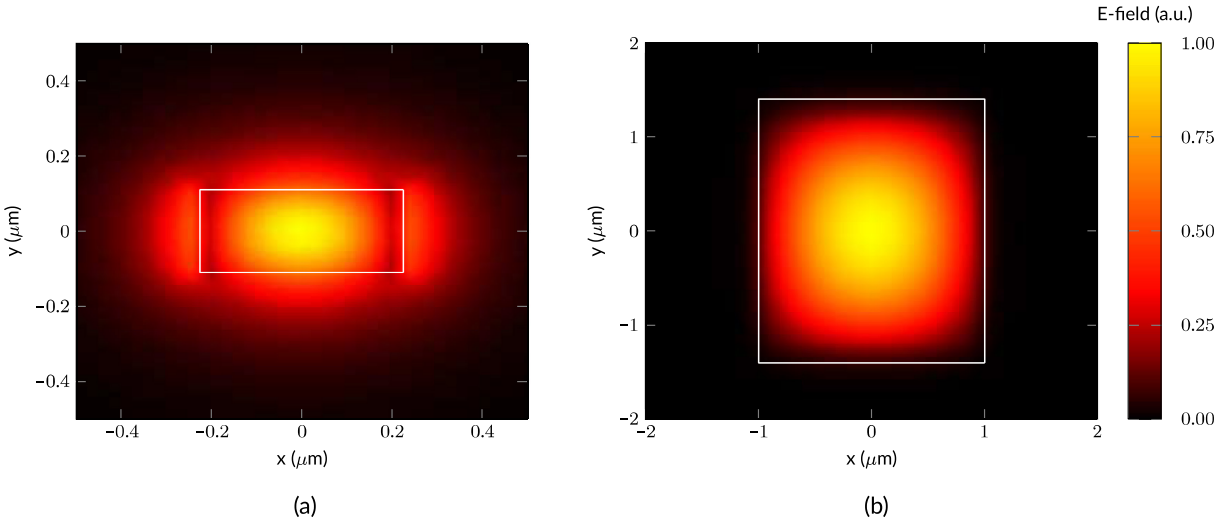


**FIGURE 5** | Simulation of the optical mode in a Si waveguide embedded in $SiO_2$ with dimensions (a) 450 nm × 220 nm and (b) 2000 nm × 2800 nm . Simulation performed with Rsoft. The waveguide section profile is represented by the white rectangle.

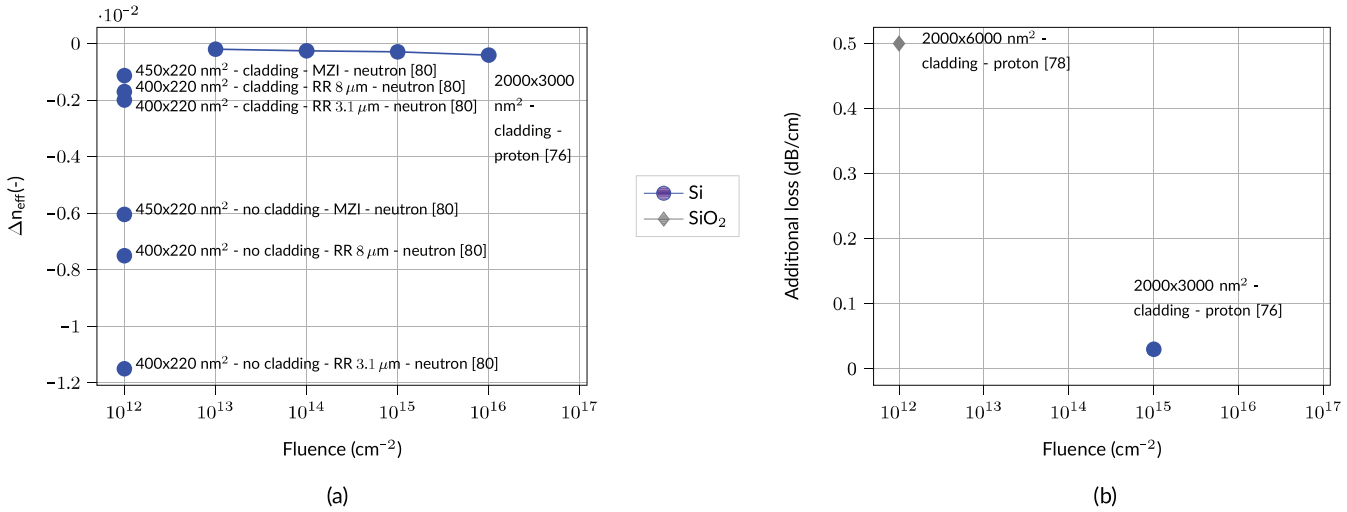


**FIGURE 6** | Summary of (a) $\Delta n_{\text{eff}}$ and (b) additional losses due to DD in different material platforms. Waveguide dimensions, presence of the cladding, and reference are noted next to the plots. $\Delta n_{\text{eff}}$ is either stated directly in the reference or inferred using Equations (1) and (2) with the available data.

is a good indication that for most applications ionization does not appear to introduce noticeable losses. The few studies that have measured additional losses are summarized in Figure 4b. To specifically target the measurement of small additional losses, Zhou et al. [76] used spirals with lengths over 10 cm, while Boynton et al. [23] used an arrayed waveguide structure. We can see that the 3000-nm-thick Si waveguide has considerably lower losses compared to the 230-nm-thick one, again showing how strong confinement is a good radiation hardening approach for Si. Another work that studied the influence of mode confinement on the additional loss was performed in [79]. Here, the authors studied three waveguide geometries: two rib waveguides with a different etch depth and a strip waveguide. The ionizing dose has the smallest impact on the geometry with the tightest confinement, which in this case is the 400 × 300 $nm^2$ rib waveguide.

**3.1.1.2 | DD.** Next, we discuss the topic of DD on passive devices. Literature results of DD-induced $\Delta n_{\text{eff}}$ and losses are summarized in Figure 6a,b, respectively. Compared to TID, there is less literature available, which shows that radiation effects on PICs is still a young field of research.

A very comprehensive study on $\Delta n_{\text{eff}}$ was performed by Zhou et al. [80] on Si waveguides, where not only the waveguide dimensions but also the bending radii were varied to study different $\Gamma_{\text{core}}$ and $\Gamma_{\text{clad}}$. Similar to TID, optical mode confinement plays an important role in $\Delta n_{\text{eff}}$. Some of the measured $\Delta n_{\text{eff}}$ are shown in Figure 6a. These measurements show that $\Delta n_{\text{eff}}$ is inversely proportional to $\Gamma_{\text{core}}$ for Si, making high-confinement waveguides more resistant to radiation. For example, when comparing devices without cladding, the 450-nm-wide waveguide of a MZI shows a smaller shift compared to the 400-nm-wide waveguide of RRs. This is also confirmed by using different ring radii: A RR with a larger ring radius, thus better mode confinement, has a smaller wavelength shift of the resonance, that is, a smaller $\Delta n_{\text{eff}}$. Similar

results are shown for cladded devices. Once again, cladded devices show higher resistance compared to unclad ones, indicating that DD also leads to surface oxidation [80]. To take advantage of the strong confinement as a radiation hardening mechanism, the same authors in a later publication showed improved radiation response with 3-μm-thick Si waveguide [76]. Studies on other material platform have been performed by Brasch et al. [81], who tested proton irradiation on SiN rings with fluences up to 1.516e101/cm$^2$, and by Piacentini et al. [78], who tested proton irradiation on $SiO_2$ waveguides, MZI, and directional couplers with fluences up to 1e121/cm$^2$. No change in $n_{eff}$ was measured in either studies. With respect to DD-induced absorption losses, only two studies reported loss measurements, which are summarized in Figure 6b. Once again, the use of a thick and high-confinement Si waveguide shows strong resilience to radiation.

**3.1.1.3 | SEE.** SEEs are the less studied radiation effect, because of the experimental challenge of producing high-energy ions and of monitoring a dynamic effect that takes place on a very short time scale. To the best of our knowledge, SEE studies on passive photonic devices are limited to Si waveguides, and are based on either simulations [82, 83] or laser-induced SEEs [84, 85].

A first method to simulate SEE on a Si waveguide was presented by Goley et al. [82], where C and Kr ion strikes were simulated. First, the carrier distribution generated by the ion passing through the waveguide needed to be simulated. Then, the carrier concentration was converted into a change of the Si optical properties using the Drude model. Finally, finite difference time domain (FDTD) simulations were performed to evaluate the impact of the ion strikes on the waveguide performance, that is, on the transmitted, reflected, and absorbed power. The lowest reported transmission for the selected ions was 91%, while the maximum phase shift was 2°. FDTD simulations are computationally heavy, and in this case also limited to a carrier distribution which is static, and thus do not include the time dynamics of a SEE. Afterwards, analytical methods have been developed to simplify the simulation and to include the time evolution of the carriers [83, 85]. Using laser-induced SEEs, it was shown that the recovery time after which the waveguide transmission is back to nominal is around 200–300 ns [85]. This corresponds to about 2000–3000 symbols in a 10-GBaud optical link. Nevertheless, this is only representative of a worst-case scenario, since the laser-induced SEEs overestimate the impact of an actual SEE. According to simulations [85], a realistic recovery time would be in the order of tens of ps. Another laser-induced SEE work was presented in [84], where the definition of optical single event transient (OSET) was given, to emphasize that the impact of this physical process is limited to the optical domain, while SEEs are commonly associated with the radiation effects on electronics.

Although simulation results have shown that in principle a 100% loss is possible [84], some of these studies have shown that losses higher than 10% are highly unlikely [82, 85]. Therefore, the real impact of OSETs is still unclear, especially because the cited studies were based on simulated tracks of a few selected ions, for example, C and Kr [82], or on analytical Gaussian distributions of the carriers [83], or on laser-induced EHPs [84, 85], but not on a specific radiation environment with its heavy ions. A recent study [86] simulated the impact of multiple heavy ions using FDTD. Atomic numbers from 1 to 35 were simulated and in a broad range of energies. Using simulated ion fluxes for typical satellite orbits, and under the assumption of vertical ion strike, it was shown that losses above 6.5% are highly unlikely and that any loss above 1.5% has an expected rate smaller than one per hour.

### 3.1.2 | Mach-Zehnder and Ring Modulators

High-speed modulators are one of the most important components of a communications system because they modulate the optical signal with the transmitted information signal. In integrated optics, modulators are typically implemented using two approaches: Mach-Zehnder modulators (MZMs) or ring modulators (RMs). High-speed modulation is typically achieved by electro-optical (EO) effects, such as the Pockels effect, the carrier density effect, and the quantum-confined Stark effect [87]. Such EO effects change the optical properties of the material, for example, refractive index and absorption, and result in modulation of the optical signal. Typical materials for high-speed integrated modulators are Si, InP, and $LiNbO_3$ [87]. In the following sections, we will report on radiation testing of MZMs and RMs. To compare different works, the normalized phase shift is typically considered as a metric. The phase shift induced by the modulator is measured over different radiation doses and normalized to the pre-irradiation phase shift at the same bias point. When the normalized phase shift drops to 0, this is equivalent to the output of the unbiased device, indicating that the modulation has no effect.

Before analyzing the impact of different effects separately, we would like to highlight a recent work [88] in which several SiPh MZMs were sent to the international space station (ISS) for six months and tested before and after their exposure to the space environment. The work reported that most of the devices can still operate with some degradation: The RF response was unchanged, and a shift in the optical response due to a change in the effective refractive index on the order of $10^{-3}$ was measured, together with a decrease in the extinction ratio from 30 to 20 dB.

**3.1.2.1 | TID.** One of the first studies in TID on a MZM was reported in [89], where SiPh MZMs were tested for use in the LHC. The measured degradation curve is shown in Figure 7a. Here the MZM was irradiated up to 1.2e8 rad, at which point the device was no longer operational. SiPh MZMs are typically realized by doping the material to achieve a p-n junction in the waveguide. By depleting the junction, the refractive index of the waveguide is changed. Therefore, the authors attributed the problem to the doping region of the MZM, meaning that the radiation had impacted the p-n junction, making depletion impossible. This was confirmed by a following simulation work [90]. In a subsequent publication, the same author showed a significant improvement in the response to TID, as shown in Figure 7a, by fabricating MZMs with a lower etch depth and a higher doping concentration [91]. Using simulation, they showed that the phase shift degradation is due to the removal of holes in

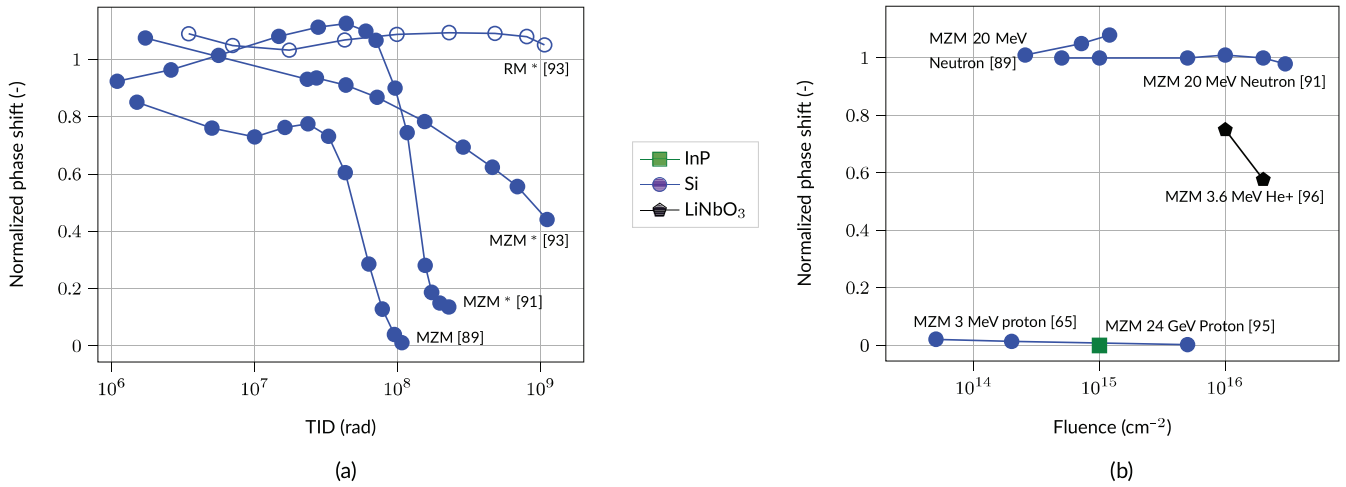


**FIGURE 7** | Summary of modulator efficiency degradation by (a) TID and (b) DD, which is given by the post-irradiation phase shift normalized by the pre-irradiation phase shift at the same biasing condition. The * indicates that multiple modulators design were analyzed in the publication, and here, the best data at room temperature are reported. Full marker stands for MZM, and empty marker for RM.

the p-doped region. The defects created by TID remove the carriers and the p-n junction cannot be depleted. The authors also measured that the degradation is faster when the bias voltage is higher, and that no change in performance was observed when the device was operated at −30 C. Further temperature studies examined the effect of post-radiation annealing and showed that full performance recovery is possible by applying a forward current [92]. A further improvement in radiation tolerance was reported in [93], where the length of the lowest concentration p-doped region, which is the most fragile point of the structure, is reduced compared to the previous generation. This results in higher resistance to radiation as shown in Figure 7a.

In the same work [93], the authors also investigated SiPh RM, which have the same p-n phase shifter junction as the MZM. Different doping concentrations were tested, and it was shown that the RM with the highest concentration is radiation tolerant, with almost no degradation up to $10^9$ rad (data shown in the plot). Another work on SiPh RM instead focused on the RF bandwidth and reported only a small bandwidth decrease from 17.75 to 16.6 GHz at $10^6$ rad. [94].

Unfortunately, no reports were found for other material platforms.

**3.1.2.2 | DD.** DD effects have been reported for both SiPh and InP modulators. In [89], SiPh MZM modulators were exposed to 20-MeV neutrons with a fluence up to 1.2e15 $cm^{-2}$. The measurement is reported in Figure 7b and shows that the device is still operational with only a small change in phase shift. The same MZM design was later exposed with fluences up to 3e16 $cm^{-2}$ [91]. Again, the device was still operational, confirming the resistance of SiPh MZM to neutron irradiation. A study using proton radiation was performed in [65], and the results are shown in Figure 7b. The protons clearly have a much greater effect than neutron radiation. This can be attributed to the fact that protons cause both DD and TID damage, so the two cannot be separated. The same study also reported the change in IL, which increased from a pre-irradiation value of 6–14.5 dB after a fluence of 5e15 $cm^{-2}$. Another study using protons was performed in [95] with InP modulators. The authors reported that the modulation response was almost absent after a fluence of 1e15 $cm^{-2}$. Finally, DD on $LiNbO_3$ has also been reported [96], where LiNbO3 thin film (10-μm-thick) modulators were irradiated with $He^+$. The results for different fluences are shown in Figure 7b. The IL was also measured and it increased from 2 to 16 dB at a fluence of 5e16 $cm^{-2}$.

**3.1.2.3 | SEE.** OSETs on MZMs were studied for the first time in [97], where laser-induced transients on a SiPh MZM were both measured and simulated. Interestingly, it was shown that the optical transient, that is, the variation in the MZM output optical power, depends on the biasing condition of the device. This operating point depends on the chosen modulation scheme. The authors showed that the OSETs are maximum when the MZM is operated in its quadrature point, while they are minima when the device is biased in the peak/null operation point. Therefore, the OSET impact on the optical communication signal depends on the modulation scheme.

### 3.1.3 | Lasers and Amplifiers

This section covers the radiation studies performed on integrated lasers and amplifiers. We discuss these devices together because a laser always includes an amplification part, thus radiation results on lasers encompass the ones on amplifiers. Not every material platform can be used to fabricate an amplifier: a direct band-gap material such as InP or GaAs is needed. For instance, optical amplification cannot be achieved with Si and SiN. Radiation studies on lasers typically focus on some key performance metrics: lasing current, output power, and lasing wavelength.

As discussed in [22], radiation studies on lasers have been conducted since 1970, but more studies are needed to test semiconductor integrated devices fabricated with standardized fabrication processes for photonic integrated circuits. Since we are interested in discussing PICs that can be fabricated in modern open-access foundries, we will focus on recent TID and DD

studies on such devices. No SEE study on these devices has been published so far to the best of the authors' knowledge.

**3.1.3.1 | TID.** Integrated InP DBR lasers were studied in [22], where three different doses of 6, 20, and 50 krad were applied. The measurement reported negligible optical power variation, and no effect on the lasing threshold. The only notable change was a red shift of the emitted lasing wavelength, which shifted of 0.171, 0.473, and 0.881 nm for the three radiation doses, respectively. Another work on integrated InP DBR laser was presented in [98], where ionizing doses up to 54 krad were applied. No change in performance attributed to radiation was found.

To complement these studies, we report also on two radiation tests on two *discrete* lasers. No significant drift was observed up to 100 krad for an InP distributed-feedback (DFB) laser in [99]. Similarly, no measurable damage up to 1e4 krad was measured in [100].

**3.1.3.2 | DD.** Some of the TID studies also performed DD tests. In the study on InP DBR lasers [98], the devices were irradiated with 60-MeV protons at fluences up to 1.5e11 $cm^{-2}$. Again, no impact attributed to radiation was measured in this work.

Similar results were reported on DFB *discrete* lasers, with no effects under 30-MeV proton irradiation up to 1e12 $cm^{-2}$ [99] and under 60-MeV proton irradiation up to 1e12 $cm^{-2}$ [101]. Instead, a higher fluence up to 5e14 $cm^{-2}$ of 0.8- and 20-MeV neutrons was used in [100]. This high fluence proved to be more damaging, with an increase in threshold current of 4 and 18 mA for the two neutron energies, respectively. Nevertheless, the damage was partially reversed by annealing.

### 3.1.4 | Photodetectors

In any optical communications system, photodiodes perform the critical function of converting the signal from the optical to the electrical domain. Similar to what was discussed earlier about lasers, radiation effects on PDs have been studied for many decades [102]. Here, we focus on discussing radiation studies on integrated PDs, which are integrated on a chip and collect light directly from a waveguide. Typically, these are defined as waveguide-integrated PDs, as opposed to normal-incidence PDs [103]. The key parameters of PDs are the responsivity, that is, the conversion rate from optical power into current, the bandwidth, and the dark current.

**3.1.4.1 | TID.** SiGe p-i-n integrated PDs for SiPh have been tested in a wide range of doses [91, 94, 104] and have shown a high tolerance to TID. No significant change in responsivity and bandwidth was measured in these studies. An increase in dark current was measured in all three studies, and the measured values normalized to the initial dark current are summarized in Figure 8a. Up to a 1.8-fold increase in dark current was measured in [91].

Integrated InP PDs were tested in [98], where the generated photocurrent was measured in different steps up to 54 krad: No significant effect was detected. Regarding the other PD metrics, to the best of the authors' knowledge, there are no other reports on integrated InP PDs. Standard *discrete* InGaAs PDs have been tested in [105] up to 50 krad and no difference in responsivity, bandwidth and dark current was found. A higher dose up to 1.7e4 krad was used in [106]. The authors concluded that InP PDs have a high tolerance to TID because no meaningful change in dark current was measured. A similar high dose study was performed in [107] where an order of magnitude increase was measured at 1e5 krad. No changes in responsivity and bandwidth were measured.

For both InP and Si PD, the high resistance to TID has been attributed to the high doping levels in the p+ region of the p-i-n junction and the large electric field separating the charges [94, 106]. This is different from the MZM and RM where there is a low doping p-region that is more easily affected by the formation of defects.

**3.1.4.2 | DD.** Not many studies are available on the DD effects of waveguide-integrated PDs. In [108], Si-Ge p-i-n PDs were tested with 14-MeV neutrons up to a fluence of 7.5e12 $cm^{-2}$.

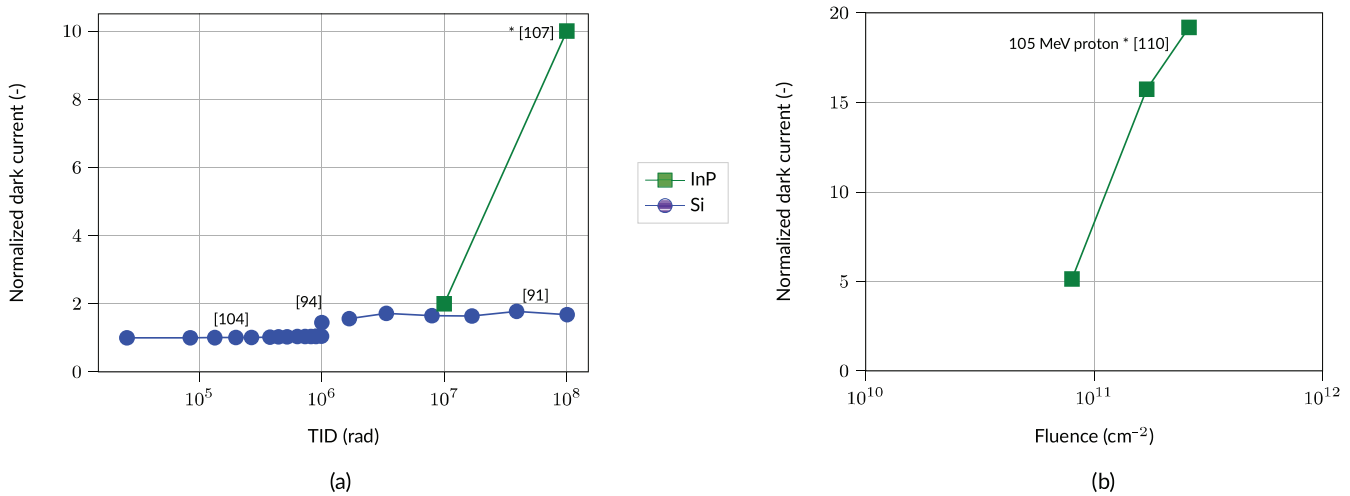


**FIGURE 8** | Summary of dark current increases in PDs from (a) TID and (b) DD. The post-irradiation dark current is normalized with the pre-irradiation dark current. References marked with * are taken from studies on *discrete* devices.

The work showed that although DD resulted in carrier removal, no meaningful change in device performance was measured. This included measurements of dark current, responsivity and bandwidth.

No studies of waveguide-integrated InP PDs were found. However, we can still discuss DD radiation tolerance based on reports from *discrete* devices. A complete compendium of DD results on InGaAs PDs was presented in [109]. Here, it was concluded that the dark current increases linearly with the DD dose and that InGaAs PDs are more than three orders of magnitude more sensitive to DD than silicon-based PDs. As an example, we report in Figure 8b some measurements on a PIN InGaAs PD with 105-MeV protons at 2.55e11 $cm^{-2}$ fluence [110]. To improve the radiation tolerance, dual-depletion region (DDR) InP / InGaAs PDs were tested where the p-i-n structure is replaced by a p-i-i-n structure [111]. These modified InP showed increased tolerance with no change in responsivity and bandwidth, and an increase in dark current of less than 2 for 50-MeV protons up to a fluence of 1e11 $cm^{-2}$. These devices were also flown to the ISS for 18 months [112] and no change in device performance was measured.

**3.1.4.3 | SEE.** A first study of single event transients (SETs) on Si-Ge PDs was performed using a pulsed laser to generate SETs in [113]. Two different detector geometries were considered, a vertical p-i-n PD and a lateral p-i-n photodiode. The laser was used to generate charges in the active region of the PD, and transient currents from the PD were recorded. Both devices exhibit current transients with amplitudes up to 10 mA. The transient duration was shorter for the vertical PD, with a full-width at half-maximum (FWHM) of about 0.4 ns, compared to a FWHM of 0.8 ns for the lateral PDs. The difference was attributed to the carrier transient time across the p-i-n junction, which is lower for the vertical PDs. Subsequently, another paper tested SETs on Si-Ge PDs, but using ion bombardment from different heavy ions in order to have a test that is a more accurate representation of the space environment [114]. Lateral p-i-n PDs were considered. Depending on the ion linear energy transfer (LET), current transients between 0.5 and 2.5 mA were measured. Interestingly, the amplitude of the transient decreases with the optical power at the input of the waveguide. This was attributed to a reduced electric field from the optically generated carriers, which in turn increases the carrier transient time and flattens the current transient over a longer period of time. As discussed in [114], the current transient can lead to a bit error if the amplitude is sufficient to pass the decision level between one bit and another.

No single event effect (SEE) studies were found on waveguide-integrated InP. A test on a *discrete* p-i-n InP PD was performed in [115]. Current transients up to 20 mA were measured, with a pulse FWHM up to 10 ns. Both the time and amplitude of these peaks are larger than those measured on Si-Ge, but this can be attributed to the much larger volume that collects the carrier: 80 μm × 80 μm × 12 μm [115] versus 0.9 μm × 0.28 μm × 15 μm [114].

### 3.1.5 | System Level

There are not many studies of radiation testing at a the system level, that is, testing multiple integrated devices together to study the combined effect on the system. In [116], an InP integrated receiver was tested. The chip included an absorber, two polarization beam splitters, two 90° hybrids and multiple high-speed PDs. The bandwidth of the receiver was tested under ionizing radiation up to 100 krad. No significant degradation was measured in the response between 1 and 30 GHz. In [117], an analytical model was used to evaluate the impact of OSET on a deep space optical communications system using pulse position modulation. It was shown that the symbol error probability increases by several orders of magnitude during the OSET, and that higher bit rates are more vulnerable. This is due to the higher number of symbols within the time window of the transient.

To conclude, a summary of the different effects induced by radiation on integrated devices is reported in Table 2.

## 3.2 | Other Space Effects

So far, we have only discussed the impact of radiation. However, there are many other challenges that a space-based system has to face, not only during its operation but also during its deployment from Earth. For instance, vibration during the launch, different temperatures in different parts of the orbit, vacuum, limited power budget. These are typically reflected in the qualification process of a system intended for space applications. In order to qualify a photonic device for space

**TABLE 2** | Summary of main radiation effects discussed in the text divided by radiation type and device category.

| Device | TID | DD | SEE |
|---|---|---|---|
| Waveguide/ring resonator/MZI | Additional loss and change in effective index | Additional loss and change in effective index | Transient additional loss and change in effective index |
| MZM/ring modulator | Decreased phase shift at same bias and/or device is no longer operational at high dose | Decreased phase shift at same bias and/or device is no longer operational | Optical power transient |
| Laser amplifier | Wavelength shift | | |
| Photodiode | Dark current increase | | Transient increase of photocurrent |

application, it has to undergo numerous tests [118]. For example, in the qualification of a laser reported in [99], 57 copies of the device were needed to complete the qualification process. This included temperature cycling, radiation testing, mechanical stress, vacuum, humidity, and life test. Another example of multiple tests is [101], where a DFB laser module underwent proton radiation testing and vibration testing. There are not many studies on the qualification of PICs and its tests other than radiation. In [116], an integrated coherent receiver, packaged in a standard butterfly package, was subjected to a series of environmental tests: thermal cycling between −5°C and 65°C over 7 days, vibration testing, shock testing, and thermal vacuum testing. Temperature cycling resulted in only minor changes in device bandwidth at frequencies above 25 GHz. No degradation was observed during shock, vibration, and thermal vacuum testing.

## 4 | Conclusions

In this paper, we have reviewed the current state of the art in using PICs for OSLs. In Section 2, the technology was briefly introduced and the advantage of using photonic integration over separate discrete optical components was discussed: the use of PICs would reduce the C-SWaP of the communications payload, thus allowing more resources on the satellite. Four material platforms, SiPh, SiN, InP, and $LiNbO_3$, were then presented and compared. The first three are already mature and available through open access services, while the last one is under development. We showed that while InP is the only platform that allows for all the components needed for optical communications, the use of multiple material platforms would allow to exploit the strengths and advantages of each material. We then showed how PICs would be integrated into an OSL terminal, and different integration approaches were discussed, for instance using a single monolithic chip or multiple chips composed of different materials. However, not every component can be integrated, and the challenges of achieving high output power, optical isolators, and circulators were presented.

Section 3 covered the effects of the space environment on PICs, with a particular focus on radiation effects. Since the available integrated devices were developed for terrestrial applications, it is critical to understand and evaluate the effects of the space environment. We analyzed the effects on four different device categories (passive waveguides, modulators, lasers and amplifiers, and photodiodes), focusing on the three radiation categories (TID, DD, SEE). Even though radiation affects the performance of the devices, we also discussed various mitigation approaches already available in the literature. For example, TID effects can be reduced by using cladding and strong confinement on waveguides, and high doping in SiPh MZM modulators. Nevertheless, as also concluded by Du [62] and by Tzintzarov et al. [61], the research on radiation effects on PICs is new and further investigations are needed, especially at the system level. Other space effects, such as temperature and vibration testing, were also briefly mentioned. While the focus of this paper was on OSLs, the space effects discussed are valid for any space application or use in any environment with high radiation levels.

In conclusion, PICs are a promising technology to be used in OSL terminals, which would allow to solve the current bottlenecks of RF communications in satellite networks. Although the research on the effects of space on PICs is new, this technology can utilize the mature and optimized components developed for the terrestrial network. Therefore, we expect this technology to be used in the near future not only for OSL but also for other space applications such as microwave photonics, spectroscopy, and LIDAR.

### Conflicts of Interest

The authors declare no conflicts of interest.

### Endnotes

[1] Amorphous silicon (a-Si) is a different material platform compared to conventional silicon photonics based on crystalline silicon (c-Si). While passive devices show similar performances, active devices are limited due to the absence of activated dopants [69]. Therefore, it was excluded from the material comparison in Section 2.2. Nevertheless, radiation studies are reported in the environmental effect comparison due to the material properties being similar to the one of c-Si.

[2] SiC is extensively used in microelectronics, but less established in the field of integrated photonics [75]. Therefore, it was excluded from the comparison.

### References


1. S. E. Miller, "Integrated Optics: An Introduction," *Bell System Technical Journal* 48, no. 7 (1969): 2059–2069, https://doi.org/10.1002/j.1538-7305.1969.tb01165.x.

2. F. Kish, V. Lal, P. Evans, et al., "System-on-Chip Photonic Integrated Circuits," *IEEE Journal of Selected Topics in Quantum Electronics* 24, no. 1 (2018): 1–20, https://doi.org/10.1109/JSTQE.2017.2717863.

3. V. Lal, J. Summers, N. Kim, et al., "Extended C-Band Tunable Multi-Channel InP-Based Coherent Transmitter PICs," *Journal of Lightwave Technology* 35, no. 7 (2017): 1320–1327, https://doi.org/10.1109/JLT.2017.2670547.

4. A. Hosseini, M. Lu, R. Going, et al., "Extended C-Band Tunable Multi-Channel InP-Based Coherent Receiver PICs," *Optics Express* 25, no. 16 (2017): 18853–18862, https://doi.org/10.1364/OE.25.018853.

5. A. Rahim, J. Goyvaerts, B. Szelag, et al., "Open-Access Silicon Photonics Platforms in Europe," *IEEE Journal of Selected Topics in Quantum Electronics* 25, no. 5 (2019): 1–18, https://doi.org/10.1109/JSTQE.2019.2915949.

6. M. Smit, K. Williams, and J. van der Tol, "Past, Present, and Future of InP-Based Photonic Integration," *APL Photonics* 4, no. 5 (2019): 50901, https://doi.org/10.1063/1.5087862.

7. M. Smit, X. Leijtens, H. Ambrosius, et al., "An Introduction to InP-Based Generic Integration Technology," *Semiconductor Science and Technology* 29, no. 8 (2014): 83001, https://doi.org/10.1088/0268-1242/29/8/083001.

8. L. M. Augustin, R. Santos, E. den Haan, et al., "InP-Based Generic Foundry Platform for Photonic Integrated Circuits," *IEEE Journal of Selected Topics in Quantum Electronics* 24, no. 1 (2018): 1–10, https://doi.org/10.1109/JSTQE.2017.2720967.

9. M. H. P. Pfeiffer, C. Herkommer, J. Liu, et al., "Photonic Damascene Process for Low-Loss, High-Confinement Silicon Nitride Waveguides," *IEEE Journal of Selected Topics in Quantum Electronics* 24, no. 4 (2018): 1–11.

10. S. Y. Siew, B. Li, F. Gao, et al., "Review of Silicon Photonics Technology and Platform Development," *Journal of Lightwave Technology* 39, no. 13 (2021): 4374–4389.

11. L. Rinaldi, F. Camponeschi, and A. Bogoni, "Space-Grade Analogue and Digital Photonics for Satellite Communications in Europe," *Journal of Lightwave Technology* 42, no. 3 (2024): 1004–1015.

12. H. Kaushal and G. Kaddoum, "Optical Communication in Space: Challenges and Mitigation Techniques," *IEEE Communications Surveys Tutorials* 19, no. 1 (2017): 57–96.

13. H. Hauschildt, S. Mezzasoma, H. L. Moeller, M. Witting, and J. Herrmann, "European Data Relay System Goes Global," in *2017 IEEE International Conference on Space Optical Systems and Applications (ICSOS)* (2017), 15–18.

14. A. Biswas, M. Srinivasan, R. Rogalin, et al., "Status of NASA's Deep Space Optical Communication Technology Demonstration," in *2017 IEEE International Conference on Space Optical Systems and Applications (ICSOS)* (2017), 23–27.

15. R. M. Calvo, J. Poliak, J. Surof, et al., "Optical Technologies for Very High Throughput Satellite Communications," in *Free-Space Laser Communications XXXI*, eds. H. Hemmati and D. M. Boroson, Vol. 10910 (SPIE, International Society for Optics and Photonics, 2019), 189–204.

16. P. Conroy, J. Surof, J. Poliak, and R. M. Calvo, "Demonstration of 40 GBaud Intradyne Transmission Through Worst-Case Atmospheric Turbulence Conditions for Geostationary Satellite Uplink," *Applied Optics* 57, no. 18 (2018): 5095–5101.

17. J. Poliak, R. M. Calvo, and F. Rein, "Demonstration of 1.72 Tbit/s Optical Data Transmission Under Worst-Case Turbulence Conditions for Ground-to-Geostationary Satellite Communications," *IEEE Communications Letters* 22, no. 9 (2018): 1818–1821.

18. A. Dochhan, J. Poliak, J. Surof, M. Richerzhagen, H. F. Kelemu, and R. M. Calvo, "13.16 Tbit/s Free-space Optical Transmission Over 10.45 km for Geostationary Satellite Feeder-Links," in *Photonic Networks; 20th ITG-Symposium* (2019), 1–3.

19. M. Ziarko, G. Terrasanta, N. Bergamasco, and J. Poliak, "Photonic Integrated Circuits for High-Throughput Optical Communications and Ranging Satellite Links," in *Free-Space Laser Communications XXXVI*, eds. H. Hemmati and B. S. Robinson, Vol. 12877 (SPIE, 2024), 128770G.

20. P. Marin-Palomo, J. N. Kemal, M. Karpov, et al., "Microresonator-Based Solitons for Massively Parallel Coherent Optical Communications," *Nature* 546, no. 7657 (2017): 274–279.

21. A. A. Jørgensen, D. Kong, M. R. Henriksen, et al., "Petabit-per-Second Data Transmission Using a Chip-Scale Microcomb Ring Resonator Source," *Nature Photonics* 16, no. 11 (2022): 798–802.

22. F. Gambini, N. Andriolli, V. Nurra, M. Chiesa, F. Petroni, and S. Faralli, "Study of Low-Dose Long-Exposure Gamma Radiation Effects on InP DBR Cavity Lasers From Generic Integration Technology," in *Applications in Electronics Pervading Industry, Environment and Society*, eds. S. Saponara and A. De Gloria (Cham: Springer International Publishing, 2019), 77–82.

23. N. Boynton, M. Gehl, C. Dallo, et al., "Gamma Radiation Effects on Passive Silicon Photonic Waveguides Using Phase Sensitive Methods," *Opt. Express* 28, no. 23 (2020): 35192–35201.

24. J. Gao, X. Han, X. Lei, and Y. Yu, "TEC Power Consumption in Laser Array Packaging," *Optical and Quantum Electronics* 49, no. 4 (2017): 139.

25. A. Carrasco-Casado and R. Mata-Calvo, "Space Optical Links for Communication Networks," *Springer Handbook of Optical Networks* (Cham: Springer International Publishing, 2020), 1057–1103.

26. L. Carroll, J.-S. Lee, C. Scarcella, et al., "Photonic Packaging: Transforming Silicon Photonic Integrated Circuits Into Photonic Devices," *Applied Sciences* 6, no. 12 (2016).

27. P. Kaur, A. Boes, G. Ren, T. G. Nguyen, G. Roelkens, and A. Mitchell, "Hybrid and Heterogeneous Photonic Integration," *APL Photonics* 6, no. 6 (2021): 61102.

28. R. Selim, R. Hoofman, M. Khoder, et al., "Silicon Photonics Open Access Foundry Services Review for Emerging Technology," in *Emerging Applications in Silicon Photonics II*, eds. C. G. Littlejohns and M. Sorel, Vol. 11880 (SPIE, 2021), 118800C.

29. A. Boes, B. Corcoran, L. Chang, J. Bowers, and A. Mitchell, "Status and Potential of Lithium Niobate on Insulator (LNOI) for Photonic Integrated Circuits," *Laser & Photonics Reviews* 12, no. 4 (2018): 1700256.

30. J. Leo, M. Hayati, F. E. Agri, et al., "Wafer-Scale Fabrication of Low-Loss Waveguides in Lithium Niobate on Insulator (LNOI) Integrated Photonics Platform," in *2022 European Conference on Optical Communication (ecoc)* (2022), 1–4.

31. Y. Jia, L. Wang, and F. Chen, "Ion-Cut Lithium Niobate on Insulator Technology: Recent Advances and Perspectives," *Applied Physics Reviews* 8, no. 1 (2021): 11307.

32. M. Baier, F. M. Soares, T. Gärtner, M. Moehrle, and M. Schell, "Fabrication Tolerant Integrated Polarization Rotator Design Using the Jones Calculus," *Journal of Lightwave Technology* 37, no. 13 (2019): 3106–3112.

33. Y. D. Gupta, G. Binet, W. Diels, O. Abdeen, T. Gaertner, M. Baier, and M. Schell, "Implementation, Modelling and Verification of High-Speed Mach-Zehnder Phase Modulators in an Open Access InP Foundry Platform," *Journal of Lightwave Technology* 41, no. 11 (2023): 3498–3504.

34. J. C. Cuello, A. Money, J. Leo, et al., "Characterization of Ring Resonators in Thin-Film Lithium Niobate on Insulator (LNOI) Photonic Integrated Circuit Platform," in *2023 Conference on Lasers and Electro-Optics Europe & European Quantum Electronics Conference (CLEO/Europe-EQEC)* (2023), 1–1.

35. A. Monney, J. Leo, G. Li, et al., "Statistical Characterization of MMI Beam Splitters on Thin Film Lithium Niobate on Insulator (LNOI) Platform at Telecom Wavelength," in *2023 Conference on Lasers and Electro-Optics Europe & European Quantum Electronics Conference (CLEO/Europe-EQEC)* (2023), 1–1.

36. D. J. Blumenthal, R. Heideman, D. Geuzebroek, A. Leinse, and C. Roeloffzen, "Silicon Nitride in Silicon Photonics," *Proceedings of the IEEE* 106, no. 12 (2018): 2209–2231.

37. C. Xiang, W. Jin, D. Huang, et al., "High-Performance Silicon Photonics Using Heterogeneous Integration," *IEEE Journal of Selected Topics in Quantum Electronics* 28, no. 3: Hybrid Integration for Silicon Photonics (2022): 1–15.

38. J. Zou, X. Ma, X. Xia, et al., "Novel Wavelength Multiplexer Using (n + 1) × (n + 1) Arrayed Waveguide Grating and Polarization-Combiner-Rotator on SOI Platform," *Journal of Lightwave Technology* 39, no. 8 (2021): 2431–2437.

39. D. Dai, Z. Wang, J. F. Bauters, M.-C. Tien, M. J. R. Heck, D. J. Blumenthal, and J. E. Bowers, "Low-Loss Si3N4 Arrayed-Waveguide Grating (De)multiplexer Using Nano-Core Optical Waveguides," *Optics Express* 19, no. 15 (2011): 14130–14136.

40. Y. Barbarin, X. J. M. Leijtens, E. A. J. M. Bente, C. M. Louzao, J. R. Kooiman, and M. K. Smit, "Extremely Small AWG Demultiplexer Fabricated on InP by Using a Double-Etch Process," *IEEE Photonics Technology Letters* 16, no. 11 (2004): 2478–2480.

41. J. Rodriguez and Y. Li, "Noise Analysis for Coherent Phase-Modulated RF Fiber-Optic Link," *Journal of Lightwave Technology* 39, no. 10 (2021): 3072–3080.

42. H. Zhao, S. Pinna, B. Song, et al., "Indium Phosphide Photonic Integrated Circuits for Free Space Optical Links," *IEEE Journal of Selected Topics in Quantum Electronics* 24, no. 6 (2018): 1–6.

43. J. Fridlander, V. Rosborough, F. Sang, et al., "Photonic Integrated Transmitter for Space Optical Communications," in *Free-Space Laser Communications XXXI*, eds. H. Hemmati and D. M. Boroson, Vol. 10910 (SPIE, 2019), 447–453.

44. C. Pham, F. Duport, R. Brenot, et al., "Modulation of a High Power Semiconductor Optical Amplifier for Free Space Communications," *Journal of Lightwave Technology* 38, no. 7 (2020): 1836–1843.

45. X. Zhao, D. L. Gac, S. Escobar-Landero, et al., "Real-Time 59.2 Tb/s Unrepeated Transmission Over 201.6 km Using Ultra-Wideband SOA as High-Power Booster," *Journal of Lightwave Technology* 41, no. 12 (2023): 3925–3931.

46. A. Ruiz-Caridad, G. Marcaud, E. Duran-Valdeiglesias, et al., "Heterogeneous Integration of Doped Crystalline Zirconium Oxide for Photonic Applications," *IEEE Journal of Selected Topics in Quantum Electronics* 28, no. 3: Hybrid Integration for Silicon Photonics (2022): 1–13.

47. P. Zhou, B. Wang, X. Wang, B. Wang, Y. He, and J. E. Bowers, "Design of an On-Chip Electrically Driven, Position-Adapted, Fully Integrated Erbium-Based Waveguide Amplifier for Silicon Photonics," *OSA Continuum* 4, no. 3 (2021): 790–814.

48. S. Liu, D. Minemura, and Y. Shoji, "Silicon-Based Integrated Polarization-Independent Magneto-Optical Isolator," *Optica* 10, no. 3 (2023): 373–378.

49. S. Alt, "Photonic Integrated Circuit (PIC) Device Structures: Background, Fabrication Ecosystem, Relevance to Space Systems Applications, and Discussion of Related Radiation Effects," (2016), NASA.

50. J. Surof, J. Poliak, R. Wolf, et al., "Validation of Kepler Time and Frequency Transfer on a Terrestrial Range of 10.45 km," in *Proceedings of the 35th International Technical Meeting of the Satellite Division of the Institute of Navigation (Ion GNSS+ 2022)* (2022), 3662–3670.

51. X. Zhang, K. Kwon, J. Henriksson, J. Luo, and M. C. Wu, "A Large-Scale Microelectromechanical-Systems-Based Silicon Photonics LiDAR," *Nature* 603, no. 7900 (2022): 253–258.

52. J. Fridlander, F. Sang, V. Rosborough, et al., "Dual Laser Indium Phosphide Photonic Integrated Circuit for Integrated Path Differential Absorption Lidar," *IEEE Journal of Selected Topics in Quantum Electronics* 28, no. 1 (2022): 1–8.

53. B. Wu, Y. Yu, J. Xiong, and X. Zhang, "Silicon Integrated Interferometric Optical Gyroscope," *Scientific Reports* 8, no. 8766 (2018): 2045–2322.

54. M. A. Krainak, M. A. Stephen, E. Troupaki, et al., "Integrated Photonics for NASA Applications," (2019).

55. F. Morichetti, G. Cavicchioli, A. Martinez, et al., "Mitigation of Atmospheric Turbulence in an Optical Free Space Link With an Integrated Photonic Processor," in *2023 Optical Fiber Communications Conference and Exhibition (OFC)* (2023), 1–3.

56. H. Mohammadhosseini, S. Roemer, P. Darmon, et al., "Photonic Integration and Integrated Microwave Photonic Technologies for Satellite Applications," in *International Conference on Space Optics – ICSO 2022*, eds. K. Minoglou, N. Karafolas, and B. Cugny, Vol. 12777, (SPIE. International Society for Optics and Photonics, 2023), 127774W.

57. C. Mitsolidou, R. B. Timens, V. Sánchez-Martínez, et al., "Microwave Photonic Filter With Reconfigurable Bandwidth and Tunable Central Frequency Aimed for Flexible Satellite Payloads in Ka-, Q-, -V Band," in *International Conference on Space Optics – ICSO 2022*, eds. K. Minoglou, N. Karafolas, and B. Cugny, Vol. 12777 (SPIE. International Society for Optics and Photonics, 2023), 127774Z.

58. H. Shu, L. Chang, Y. Tao, et al., "Microcomb-Driven Silicon Photonic Systems," *Nature* 605, no. 7910 (2022): 457–463.

59. M.-A. Martinod, B. Norris, P. Tuthill, et al., "Scalable Photonic-Based Nulling Interferometry With the Dispersed Multi-Baseline GLINT Instrument," *Nature Communications* 12, no. 1 (2021).

60. E. G. Stassinopoulos and J. P. Raymond, "The Space Radiation Environment for Electronics," *Proceedings of the IEEE* 76, no. 11 (1988): 1423–1442.

61. G. N. Tzintzarov, S. G. Rao, and J. D. Cressler, "Integrated Silicon Photonics for Enabling Next-Generation Space Systems," *Photonics* 8, no. 4 (2021).

62. Q. Du, "High Energy Radiation Damage on Silicon Photonic Devices: A Review," *Optical Materials Express* 13, no. 2 (2023): 403–412.

63. R. Baumann and K. Kruckmeyer, "Radiation Handbook for Electronics," (2019), Available on ti.com (https://www.ti.com/applications/industrial/aerospace-defense/technical-documents.html).

64. ECSS, "Total Dose Steady-State Irradiation Test Method," (2016), ESCC Basic Specification No. 22900, Issue 5.

65. C. Han, Z. Hu, Y. Tao, et al., "Proton Radiation Effects on High-Speed Silicon Mach-Zehnder Modulators for Space Application," *Science China Information Sciences* 65, no. 12 (2022): 222401.

66. M. A. Xapsos, P. M. O'Neill, and T. P. O'Brien, "Near-Earth Space Radiation Models," *IEEE Transactions on Nuclear Science* 60, no. 3 (2013): 1691–1705.

67. W. Bogaerts, P. De Heyn, T. Van Vaerenbergh, et al., "Silicon Microring Resonators," *Laser & Photonics Reviews* 6, no. 1 (2012): 47–73.

68. G. Brunetti, I. McKenzie, F. Dell'Olio, M. N. Armenise, and C. Ciminelli, "Measured Radiation Effects on InGaAsP/InP Ring Resonators for Space Applications," *Optics Express* 27, no. 17 (2019): 24434–24444.

69. A. M. Agarwal and J. Michel, "Amorphous Silicon in Microphotonics," in *Springer Handbook of Glass*, eds. J. D. Musgraves, J. Hu, and L. Calvez (Cham: Springer International Publishing, 2019): 1483–1493.

70. Q. Du, Y. Huang, O. Ogbuu, et al., "Gamma Radiation Effects in Amorphous Silicon and Silicon Nitride Photonic Devices," *Optics Letters* 42, no. 3 (2017): 587–590.

71. G. N. Tzintzarov, J. W. Teng, D. Nergui, et al., "Direct Measurement of Total-Ionizing-Dose-Induced Phase Shifts in Commercially Available, Integrated Silicon-Photonic Waveguides," *IEEE Transactions on Nuclear Science* 70, no. 8 (2023): 2116–2124.

72. S. Bhandaru, S. Hu, D. M. Fleetwood, and S. M. Weiss, "Total Ionizing Dose Effects on Silicon Ring Resonators," *IEEE Transactions on Nuclear Science* 62, no. 1 (2015): 323–328.

73. P. Dumon, R. Kappeler, D. Barros, I. McKenzie, D. Doyle, and R. Baets, "Measured Radiation Sensitivity of Silica-on-Silicon and Silicon-on-Insulator Micro-Photonic Devices for Potential Space Application," in *Photonics for Space Environments X*, ed. E. W. Taylor, Vol. 5897 (SPIE, 2005), 58970D.

74. Q. Du, J. Michon, B. Li, et al., "Real-Time, In Situ Probing of Gamma Radiation Damage With Packaged Integrated Photonic Chips," *Photonics Research* 8, no. 2 (2020): 186–193.

75. S. Castelletto, A. Peruzzo, C. Bonato, et al., "Silicon Carbide Photonics Bridging Quantum Technology," *ACS Photonics* 9, no. 5 (2022): 1434–1457.

76. Y. Zhou, D. Lv, D. Bi, et al., "Radiation-Hardened Silicon Photonic Passive Devices on a 3 $\mu$m Waveguide Platform Under Gamma and Proton Irradiation," *Optics Express* 30, no. 10 (2022): 16921–16930.

77. S. Grillanda, V. Singh, V. Raghunathan, et al., "Gamma Radiation Effects on Silicon Photonic Waveguides," *Optics Letters* 41, no. 13 (2016): 3053–3056.

78. S. Piacentini, T. Vogl, G. Corrielli, P. K. Lam, and R. Osellame, "Space Qualification of Ultrafast Laser-Written Integrated Waveguide Optics," *Laser & Photonics Reviews* 15, no. 2 (2020): 2000167.

79. I. Reghioua, S. Girard, A. Morana, et al., "Radiation Effects on Si-Photonics-Integrated Passive Devices: Postirradiation Measurements," *IEEE Transactions on Nuclear Science* 70, no. 8 (2023): 1973–1981.

80. Y. Zhou, D. Bi, S. Wang, et al., "High Energy Irradiation Effects on Silicon Photonic Passive Devices," *Optics Express* 30, no. 3 (2022): 4017–4027.

81. V. Brasch, Q.-F. Chen, S. Schiller, and T. J. Kippenberg, "Radiation Hardness of High-Q Silicon Nitride Microresonators for Space Compatible Integrated Optics," *Optics Express* 22, no. 25 (2014): 30786–30794.

82. P. S. Goley, Z. E. Fleetwood, and J. D. Cressler, "Potential Limitations on Integrated Silicon Photonic Waveguides Operating in a Heavy Ion Environment," *IEEE Transactions on Nuclear Science* 65, no. 1 (2018): 141–148.

83. L. D. Ryder, R. D. Schrimpf, R. A. Reed, and S. M. Weiss, "Radiation-Induced Transient Response Mechanisms in Photonic Waveguides," *IEEE Transactions on Nuclear Science* 69, no. 3 (2022): 546–557.

84. G. N. Tzintzarov, A. Ildefonso, J. W. Teng, et al., "Optical Single-Event Transients Induced in Integrated Silicon-Photonic Waveguides by Two-Photon Absorption," *IEEE Transactions on Nuclear Science* 68, no. 5 (2021): 785–792.

85. P. S. Goley, G. M. Maggioni, E. Preisler, and J. D. Cressler, "Modeling Transient Loss Due to Ionizing Particles in Silicon Photonic Waveguides," *IEEE Transactions on Nuclear Science* 69, no. 3 (2022): 518–526.

86. G. Terrasanta, M. W. Ziarko, N. Bergamasco, M. Poot, and J. Poliak, "Simulating Optical Single Event Transients on Silicon Photonic Waveguides for Satellite Communication," *IEEE Transactions on Nuclear Science* (2024).

87. K. Liu, C. R. Ye, S. Khan, and V. J. Sorger, "Review and Perspective on Ultrafast Wavelength-Size Electro-Optic Modulators," *Laser & Photonics Reviews* 9, no. 2 (2015): 172–194.

88. D. Mao, L. Chang, H. Lee, et al., "Cosmic Radiation Effect on Silicon Photonic Mach-Zehnder Modulator," in *2022 Conference on Lasers and Electro-Optics (CLEO)* (2022), 1–2.

89. S. Seif El Nasr-Storey, F. Boeuf, C. Baudot, et al., "Effect of Radiation on a Mach–Zehnder Interferometer Silicon Modulator for HL-LHC Data Transmission Applications," *IEEE Transactions on Nuclear Science* 62, no. 1 (2015): 329–335.

90. S. Seif El Nasr-Storey, F. Boeuf, C. Baudot, et al., "Modeling TID Effects in Mach-Zehnder Interferometer Silicon Modulator for HL-LHC Data Transmission Applications," *IEEE Transactions on Nuclear Science* 62, no. 6 (2015): 2971–2978.

91. M. Zeiler, S. S. El Nasr-Storey, S. Detraz, et al., "Radiation Damage in Silicon Photonic Mach–Zehnder Modulators and Photodiodes," *IEEE Transactions on Nuclear Science* 64, no. 11 (2017): 2794–2801.

92. A. Kraxner, S. Detraz, L. Olantera, et al., "Investigation of the Influence of Temperature and Annealing on the Radiation Hardness of Silicon Mach–Zehnder Modulators," *IEEE Transactions on Nuclear Science* 65, no. 8 (2018): 1624–1631.

93. M. Lalović, C. Scarcella, A. Bulling, et al., "Ionizing Radiation Effects in Silicon Photonics Modulators," *IEEE Transactions on Nuclear Science* 69, no. 7 (2022): 1521–1526.

94. G. B. Hoffman, M. Gehl, N. J. Martinez, et al., "The Effect of Gamma Radiation Exposure on Active Silicon Photonic Device Performance Metrics," *IEEE Transactions on Nuclear Science* 66, no. 5 (2019): 801–809.

95. D. Gajanana, M. van Beuzekom, M. Smit, and X. Leijtens, "Irradiation Tests on InP Based Mach Zehnder Modulator," *Journal of Instrumentation* 8, no. 2 (2013): C02025–C02025.

96. H.-C. Huang, J. I. Dadap, G. Malladi, I. Kymissis, H. Bakhru, and R. M. Osgood, "Helium-Ion-Induced Radiation Damage in Linbo3 Thin-Film Electro-Optic Modulators," *Optics Express* 22, no. 16 (2014): 19653–19661.

97. M. Hosseinzadeh, J. W. Teng, D. Nergui, et al., "Analysis of Optical Single-Event Transients in Integrated Silicon Photonics Mach-Zehnder Modulators for Space-Based Optical Communications," *IEEE Transactions on Nuclear Science* (2023): 1–1.

98. A. Pérez-Serrano, A. Soria-Gómez, D. Poudereux, et al., "Evaluation of Radiation Hardness of InP-Based Photonic Integrated Circuits for Space Applications," in *International Conference on Space Optics – ICSO 2022*, eds. K. Minoglou, N. Karafolas, and B. Cugny, Vol. 12777 (SPIE. International Society for Optics and Photonics, 2023), 127776F.

99. P. Henderson, A. Norman, J. MacDougall, et al., "Space Validation of 1550 nm DFB Laser Diode Module," in *International Conference on Space Optics – ICSO 2018*, eds. Z. Sodnik, N. Karafolas, and B. Cugny, Vol. 11180 (SPIE. International Society for Optics and Photonics, 2019), 1976–1989.

100. K. Gill, R. Grabit, J. Troska, and F. Vasey, "Radiation Hardness Qualification of InGaAsP/InP 1310 nm Lasers for the CMS Tracker Optical Links," *IEEE Transactions on Nuclear Science* 49, no. 6 (2002): 2923–2929.

101. M. Faugeron, B. Benazet, A. Maho, et al., "High-Performance DFB Laser Module for Space Applications: the FP7 HiPPO Achievements From Chip Fabrication to System Validation," in *International Conference on Space Optics – ICSO 2018*, eds. Z. Sodnik, N. Karafolas, and B. Cugny, Vol. 11180 (SPIE. International Society for Optics and Photonics, 2019), 111803J.

102. C. E. Barnes, "Radiation Effects on Light Sources and Detectors," in *Radiation Effects on Optical Materials*, ed. P. W. Levy, Vol. 0541 (SPIE, 1985), 138–149.

103. J. Michel, J. Liu, and L. C. Kimerling, "High-Performance Ge-on-Si Photodetectors," *Nature Photonics* 4, no. 8 (2010): 527–534.

104. P. S. Goley, G. N. Tzintzarov, S. Zeinolabedinzadeh, et al., "Total Ionizing Dose Effects in 70-GHz Bandwidth Photodiodes in a SiGe Integrated Photonics Platform," *IEEE Transactions on Nuclear Science* 66, no. 1 (2019): 125–133.

105. A. M. Joshi and S. Datta, "Space Qualification of InGaAs Photodiodes and Photoreceivers," in *Sensors and Systems for Space Applications XI*, eds. K. D. Pham and G. Chen, Vol. 10641 (SPIE, 2018), 106410K.

106. D. L. Hansen, M. J. Robinson, and F. Lu, "Total-Dose Effects in InP Devices," in *2007 IEEE Radiation Effects Data Workshop* (2007), 68–72.

107. S. Seif El Nasr-Storey, S. Detraz, L. Olantera, et al., "High Dose Gamma Irradiation of Lasers and P-I-N Photodiodes for HL-LHC Data Transmission Applications," *IEEE Transactions on Nuclear Science* 60, no. 4 (2013): 2518–2524.

108. P. S. Goley, N. A. Dodds, M. Frounchi, G. N. Tzintzarov, R. N. Nowlin, and J. D. Cressler, "Response of Waveguide-Integrated Germanium-on-Silicon P-I-N Photodiodes to Neutron Displacement Damage," *IEEE Transactions on Nuclear Science* 67, no. 1 (2020): 296–304.

109. O. Gilard, L. S. How, A. Delbergue, et al., "Damage Factor for Radiation-Induced Dark Current in InGaAs Photodiodes," *IEEE Transactions on Nuclear Science* 65, no. 3 (2018): 884–895.

110. R. Aniceto, R. Milanowski, S. Moro, K. Cahoy, and G. Schlenvogt, "Proton Radiation Effects on Hamamatsu InGaAs Pin Photodiodes," in *2017 17th European Conference on Radiation and Its Effects on Components and Systems (RADECS)* (2017), 1–6.

111. A. M. Joshi, S. Datta, J. Mertz, et al., "In-Situ Proton Radiation Testing of 2.4 Micron Wavelength Extended InGaAs Photodiodes at Dry Ice and Room Temperatures," in *Laser Radar Technology and Applications XXVI*, eds. M. D. Turner and G. W. Kamerman, Vol. 11744 (SPIE, 2021), 117440C.

112. A. Joshi, N. Prasad, and S. Datta, "Successful Space Flight of High-Speed InGaAs Photodiode Onboard the International Space Station," (2017), Iss r&d conference 2017.

113. L. D. Ryder, K. L. Ryder, A. L. Sternberg, et al., "Single-Event Transient Response of Vertical and Lateral Waveguide-Integrated Germanium Photodiodes," *IEEE Transactions on Nuclear Science* 68, no. 5 (2021): 801–806.

114. G. N. Tzintzarov, J. W. Teng, A. N. Bozovich, G. R. Allen, D. Nergui, Y. A. Mensah, and J. D. Cressler, "Single-Event Transients in a Commercially Available, Integrated Germanium Photodiode for Silicon Photonic Systems," *IEEE Transactions on Nuclear Science* 69, no. 3 (2022): 527–533.

115. M. Hofbauer, B. Steindl, K. Schneider-Hornstein, B. Goll, K.-O. Voss, and H. Zimmermann, "Single-Event Transients in a Pin Photodiode and a Single-Photon Avalanche Diode Integrated in 0.35$\mu$ m CMOS," in *2018 18th European Conference on Radiation and Its Effects on Components and Systems (RADECS)* (2018), 1–5.

116. C. C. Foy, J. Minch, D. Feld, et al., "Qualifying an Integrated Coherent Receiver for Space Applications," in *Free-Space Laser Communications XXXIV*, eds. H. Hemmati and B. S. Robinson, Vol. 11993 (SPIE, 2022), 1199306.

117. G. N. Tzintzarov, J. W. Teng, A. Ildefonso, and J. D. Cressler, "Analysis of the Impact of Radiation-Induced Optical Transients on Deep-Space Optical Communications Systems Using PPM," in *Optical Fiber Communication Conference (OFC) 2021* (Optical Society of America, 2021), F4E.5.

118. N. Karafolas, J. M. P. Armengol, and I. Mckenzie, "Introducing Photonics in Spacecraft Engineering: ESA's Strategic Approach," in *2009 IEEE Aerospace Conference* (2009), 1–15.

## Appendix A

### Radiation Review

Table A1 summarizes the radiation studies listed in this paper, categorized by radiation effect, technology platform, and device category. Table A2 summarizes the radiation studies listed in the paper, categorized by commercial foundry and technology platform.

**TABLE A1** | Literature references about radiation used in this work categorized by radiation effect, technology platform, and device category.

| Device | Technology platform | TID | DD | SEE |
|---|---|---|---|---|
| Waveguide/ring resonator/MZI | InP | [68] | | |
| | SiPh | [23, 71–73, 76, 79] | [76, 80] | [84, 85, 82[a]], [83][a], [86][a] |
| | SiN | [70] | [81] | |
| | LNOI | | | |
| | a-Si | [70, 77] | | |
| | SiC | [74] | | |
| | $SiO_2$ | [78] | [78] | |
| Laser/amplifier | InP | [22, 98, 99[b]], [100][b] | [98], 99[b], [101][b], [100][b] | |
| MZM/ring modulator | InP | | [95] | |
| | SiPh | [89, 91–94],90[a] | [65, 89, 91] | [97] |
| | LNOI | | [96] | |
| Photodiode | InP | [98, 106[b], [105][b], [107][b] | [109][b], [110][b], [111][b], [112][b] | [115][b] |
| | SiPh | [91, 94, 104] | [108] | [113, 114] |
| System | InP | [116] | | |
| | SiPh | | | [117][a] |

[a]Simulation.
[b]*Discrete* device.

**TABLE A2** | Literature references about radiation used in this work categorized by commercial foundry and technology platform.

| Foundry | Technology platform | Reference |
|---|---|---|
| Oclaro | InP | [22] |
| SMART Photonics | InP | [95, 98] |
| CEA-Leti | SiPh | [79] |
| Global Foundries | SiPh | [84, 97, 108, 114] |
| Imec | SiPh | [91–93, 113] |
| IHP | SiPh | [104] |
| Sandia | SiPh | [94] |
| Tower Semiconductor | SiPh | [71] |